Monthly Notices of the ROYAL ASTRONOMICAL SOCIETY

MNRAS **525,** 1498–1519 (2023)
Advance Access publication 2023 July 27

https://doi.org/10.1093/mnras/stad2226

Evidence for mass-dependent peculiar velocities in compact object binaries: towards better constraints on natal kicks

Yue Zhao [1]★ Poshak Gandhi [1] Cordelia Dashwood Brown,[1] Christian Knigge [1] Phil A. Charles,[1] Thomas J. Maccarone[2] and Pornisara Nuchvanichakul [1,3]

[1]*School of Physics & Astronomy, University of Southampton, Highfield, Southampton SO17 1BJ, UK*
[2]*Department of Physics & Astronomy, Texas Tech University, Lubbock, TX 79410-1051, USA*
[3]*Department of Physics and Materials Science, Faculty of Science, Chiang Mai University, Chiang Mai, 50200, Thailand*

Accepted 2023 July 20. Received 2023 July 20; in original form 2023 April 5

ABSTRACT

We compile a catalogue of low-mass and high-mass X-ray binaries, some recently reported binaries that likely host a neutron star (NS) or a black hole (BH), and binary pulsars (a pulsar and a non-degenerated companion) that have measured systemic radial velocities (γ). Using *Gaia* and radio proper motions together with γ, we integrate their Galactic orbits and infer their post-supernova (post-SN) 3D peculiar velocities ($v_{\rm pec}^{z=0}$ at Galactic plane crossing); these velocities bear imprints of the natal kicks that compact objects received at birth. With the sample totalling 85 objects, we model the overall distribution of $v_{\rm pec}^{z=0}$ and find a two-component Maxwellian distribution with a low- ($\sigma_v \approx 21\,{\rm km s^{-1}}$) and a high-velocity ($\sigma_v \approx 107\,{\rm km s^{-1}}$) component. A further comparison between distributions of binary subgroups suggests that binaries hosting high-mass donors/luminous companions mostly have $v_{\rm pec}^{z=0} \lesssim 100\,{\rm km s^{-1}}$, while binaries with low-mass companions exhibit a broader distribution that extends up to $\sim 400\,{\rm km s^{-1}}$. We also find significant anticorrelations of $v_{\rm pec}^{z=0}$ with binary total mass ($M_{\rm tot}$) and orbital period ($P_{\rm orb}$), at over 99 per cent confidence. Specifically, our fit suggests $v_{\rm pec}^{z=0} \propto M_{\rm tot}^{-0.5}$ and $v_{\rm pec}^{z=0} \propto P_{\rm orb}^{-0.2}$. Discussions are presented on possible interpretation of the correlations in the context of kinematics and possible biases. The sample should enable a range of follow-up studies on compact object binary kinematics and evolution.

Key words: parallaxes – proper motions – stars: black holes – stars: neutron – supernovae: general.

1 INTRODUCTION

The deaths of massive stars can deliver an extra acceleration to their remnant black holes (BHs; Brandt, Podsiadlowski & Sigurdsson 1995; Jonker & Nelemans 2004) and neutron stars (NSs; Trimble 1971; Lyne, Anderson & Salter 1982; Lyne & Lorimer 1994) at the instant of supernovae (SNe). This impulse, termed as natal kick or NK, connects SN mechanisms to the kinematics of compact objects, providing a way of constraining multiple aspects of SN models. For example, NKs can be a result of recoil due to baryonic ejecta at the instant of SNe (Blaauw 1961; Brandt & Podsiadlowski 1995; Nelemans, Tauris & van den Heuvel 1999), or, in later stages, due to anisotropicity in gravitational attraction of compact object by the asymmetric ejecta (Janka 2013, 2017) – NKs could therefore be related to ejecta mass and/or morphology, and some observational support for this scenario exists (Holland-Ashford et al. 2017). The recoil momentum can also be contributed by asymmetric neutrino emission, typically in highly magnetised and hot nuclear matter of nascent NSs, where neutrino emissivity and opacity is dependent on its direction relative to local magnetic fields (Chugai 1984; Dorofeev, Rodionov & Ternov 1985; Arras & Lai 1999). More fundamentally, causes of asymmetries in ejecta or neutrino emission are related to intrinsic hydrodynamical processes (see Lai 2004, for a review).

Observations of NSs or BHs or binaries that host them have put some constraints on NKs. Pulsars have long been observed to have high space velocities (mean velocity of $\approx 300\,{\rm km s^{-1}}$) relative to their presumed OB progenitors (Gunn & Ostriker 1970; Lyne & Lorimer 1994; Hobbs et al. 2005; Kapil et al. 2023), suggestive of high NKs, although a relatively low-velocity (mean $\approx 120\,{\rm km s^{-1}}$) population is also present (Brisken et al. 2003; Verbunt, Igoshev & Cator 2017; Igoshev 2020). While isolated NSs might be observed as radio pulsars, constraining the kinematics of isolated BHs can only be done in rare microlensing events (Andrews & Kalogera 2022; Lam et al. 2022; Sahu et al. 2022) or via accretion from the interstellar medium (Fujita et al. 1998; Maccarone 2005). X-ray binaries (XRBs) that host an NS or BH are advantageous targets in this regard, because the luminous companion can be used to constrain orbital parameters and track systemic motion; inference on NKs can therefore be made using observed peculiar motions of BH and NS XRBs in Galactic potential (e.g. Mirabel et al. 2001; Atri et al. 2019; Gandhi et al. 2019; Fortin et al. 2022; O'Doherty et al. 2023) and results of binary evolutionary models (e.g. Fragos et al. 2009; Kimball et al. 2022).

In addition to the kinematic inferences of NKs, there have also been indirect constraints from other perspectives. The eccentric ($e \gtrsim 0.3$) orbits of Be XRBs are indicative of large NKs (Brandt &

★ E-mail: yue.zhao@soton.ac.uk

Podsiadlowski 1995; Verbunt & van den Heuvel 1995; van den Heuvel et al. 2000), but there might also be a separate population of long-orbit and low-eccentricity high-mass X-ray binaries (HMXBs) that argue against a large NK (Pfahl et al. 2002b; Podsiadlowski et al. 2004; Knigge, Coe & Podsiadlowski 2011). The retention fraction of NSs in globular clusters is another indicator of NK magnitude: even a moderate number of NSs (in XRBs) is at odds with large NKs derived from pulsar observations as they are hard to be retained by typical escape velocities of globular clusters ($\lesssim 50\,\mathrm{km s^{-1}}$; Pfahl, Rappaport & Podsiadlowski 2002a; Smits et al. 2006; Ivanova et al. 2008).

In this work, we compile a more comprehensive sample of binaries that host an NS or BH (so they have experienced only one NK), calculate their peculiar motion in Galactic potential, and investigate possible dependencies of their observed peculiar velocities on binary total mass and other orbital parameters. The sample includes binary pulsars (a binary that hosts a pulsar and a non-degenerate companion or sometimes a white dwarf), low-mass XRBs (LMXBs) and HMXBs, and non-interacting (NI) binaries hosting NSs or BHs. In Section 2, we describe sample compilation, inference of distances, and calculation of peculiar velocities; in Section 3, we describe statistical methods used in our analyses and present the results; in Section 4, we discuss possible interpretation of and possible biases in the results; and in Section 5, we summarize the results and draw conclusions.

2 METHODOLOGY

2.1 The raw sample

To construct our sample, we start by concatenating compilations of different types of BH or NS binaries. For XRBs, we use the BlackCAT catalogue[1] (Corral-Santana et al. 2016, and references therein) and the catalogues of LMXBs and HMXBs compiled by Liu, van Paradijs & van den Heuvel (2007) and Liu, van Paradijs & van den Heuvel (2006), respectively (L06 and L07 hereafter), and a recent HMXB catalogue compiled by Fortin et al. (2023). Additionally, we include binaries that have been recently suggested to host BHs or NSs, including 2MASS J05215658 + 4359220 (Thompson et al. 2019, J052156), AS 386 (Khokhlov et al. 2018), HD 96 670 (Gomez & Grindlay 2021), 2XMM J125556.57 + 565846.4 (Mazeh et al. 2022, J125556), Gaia BH1 (El-Badry et al. 2023b; Chakrabarti et al. 2023), Gaia BH2 (Tanikawa et al. 2022; El-Badry et al. 2023a), LAMOST J112306.9 + 400736 (Yi et al. 2022, J112306), 2MASS J15274848 + 3536572 (Lin et al. 2023, J15274848), 2MASS J06163552 + 2319094 (Yuan et al. 2022, J06163552), and LAMOST J235456.76 + 335625.7 (Zheng et al. 2022, J235456). Finally, we also include a sample of binary pulsars selected from the Australia Telescope National Facility (ATNF version 1.67) pulsar catalogue[2] (Manchester et al. 2005), using `type(binary)` to select pulsars with one or more companions.

2.2 Binaries excluded

We exclude XRBs in globular clusters from our sample because their present-day velocities do not reflect the kinematics and SN kicks at birth. Most XRBs in globular clusters are thought to form via dynamical encounters between compact objects and normal stars (e.g. Fabian, Pringle & Rees 1975; Hills 1976; Camilo & Rasio 2005), after which the systems have lost track of the SN impact. Even if there are XRBs in globular clusters that formed through primordial binary evolution (similar to field XRBs), their systemic motion could have been greatly modified by encounters after formation. We also do not consider double pulsars as their progenitors might have experienced two SNe, which make them distinct from the single-degenerate binaries in our sample.

2.3 Binary type names

Binaries in our compilation are labelled based on their compact objects, NS or BH, and the mass of the non-degenerate companions, either low-mass (LM) or high-mass (HM) according to classification in the literature; for non-interacting (NI) binaries, we consider those with non-degenerate companion mass below $2\,\mathrm{M_\odot}$ as LM, while those above as HM. Concretely, there are BH or NS LMXBs and HMXBs (labelled: BH- or NS-LMXBs or HMXBs), LM or HM NI binaries that host BH or NS (BH or NS-HMNI/LMNI). Pulsars are labelled separately from the XRBs by the mass of their non-degenerate companions (as LM or HM-PSR), although they are evolutionarily related to NS XRBs.

2.4 Binary masses and orbital periods

We also include available component masses and orbital periods from the literature. For binary component masses, we use the following notation: in any binary, M_1 is used to denote mass of the compact object (either a BH or a NS), while M_2 refers to the mass of the non-degenerate component: for XRBs, it refers to the mass donor; and for NIs, this is the luminous component. $M_{\rm tot} = M_1 + M_2$ is the total mass of a binary. For binaries that host an NS, we assume a canonical NS mass (M_1) of $1.4\,\mathrm{M_\odot}$ when there are no constraints in the literature. We denote orbital period by $P_{\rm orb}$, as distinct from the value at time of SN ($P_{\rm orb,\,SN}$) used in the discussion sections (Section 4). A list of notations is presented in Appendix D (available online).

2.5 Identification with *Gaia*

We cross-match literature positions of our sample with source positions in *Gaia* Data Release 3 (Gaia Collaboration 2016, 2023). Since position uncertainties are not consistently estimated and some are unavailable, we use a relatively large search radius of 2 arcsec to find potential counterparts. Inevitably, some binaries in our list have multiple *Gaia* sources within the search radius; we therefore further compare their literature astrometric (available for some PSRs and XRBs) and photometric properties (of the optical counterparts) to those measured by *Gaia*, manually removing unlikely matches.

The HMXBs are cross-checked with Fortin et al. (2022), who complemented L06 with the latest *INTEGRAL* catalogue (Bird et al. 2016), compiling a list of 58 unambiguous *Gaia* identifications with Galactic HMXBs. For LMXBs, Gandhi et al. (2019) reported a list of 18 matches dynamically confirmed BH systems with *Gaia* DR2, including at most 16 BH-LMXBs; all their matches are confirmed by our search; a larger catalogue of *Gaia* (DR2) counterparts to LMXBs is summarized in Arnason et al. (2021), where a total of 32 LMXBs are identified. Jennings et al. (2018) cross-matched the binary pulsars from the ATNF with *Gaia* DR2, giving a total 22 binary pulsars that have confident *Gaia* counterparts; for this work, we exclude the extragalactic PSR J0045–7319 (Storm et al. 2004), and the triple system PSR J0337+1715 (Ransom et al. 2014). Finally, we also

[1] https://www.astro.puc.cl/BlackCAT/index.php
[2] https://www.atnf.csiro.au/research/pulsar/psrcat/

cross-check our compilation of NS-LMXBs and binary pulsars with O'Doherty et al. (2023).

The identified Gaia `source_id` values are further cross-checked with sources in the `gaiadr3.nss_two_body_orbit` table. This table contains sources whose astrometric solution is compatible with a two-body system; compared to the single-body solutions in the main table, some bright sources could have much more constrained parameters with a two-body model. Three of our sources are also in this table, including Gaia BH1, Gaia BH2, and J125556; however, only Gaia BH1 and BH2 have derived parallaxes and proper motions. We thus adopt two-body solution for these two sources while using solutions in the main table for the other binaries. Parallaxes from the main *Gaia* table are corrected for zeropoint offset using the GAIADR3_ZEROPOINT package[3] (Lindegren et al. 2021) except for Gaia BH1 and BH2 whose parallaxes are from non-single star solutions.

2.5.1 *New binary pulsar matches with* Gaia *DR3*

Our positional match confirms all confident counterparts in Jennings et al. (2018) and finds seven new matches; four of these matches have a literature systemic radial velocity so are included for our calculation and analyses (Section 2.7). We therefore further investigate the four pulsars by comparing literature (from ATNF) and *Gaia* astrometry and searching for identification in literature. Here we summarise the confident matches.

PSR J1306–4035 is a millisecond pulsar (MSP) that was discovered by the SUrvey for Pulsars and Extragalactic Radio Bursts (Keane et al. 2018). Linares, Shahbaz & Casares (2018) discovered a variable optical source (SSS J130656.3–403522) within the radio error circle (≈7 arcsec); the source is modulated at the same period (P ≈1.1 d) as its X-ray flux, confirming its association with the pulsar. We found that the *Gaia* source 6 140 785 016 794 586 752 is within the 0.36″ error circle (combining positional error in Linares et al. (2018) and in *Gaia*), and the *Gaia* G-band magnitude (18.09) is consistent with the V-band magnitudes reported in Linares et al. (2018, 17.4–18.4); we therefore consider this match genuine.

PSR J1622–0315 is a MSP discovered in Fermi unassociated sources (Sanpa-Arsa 2016). The orbital light curve is modulated at half of its orbital period (≈0.16 d), varying between $R = 19.1$ and 19.4. There is only one *Gaia* source, 4358428942492430336, in our search radius. This source is 0.07 arcsec away from the nominal position and has a *Gaia* G-band magnitude of 19.21, consistent with the observed light curve in Sanpa-Arsa (2016). This match is therefore confident.

PSR J1653–0158 is a fast-spinning ($P_{\rm spin} = 1.97$ ms) and very compact ($P_{\rm orb} = 75$ min) binary pulsar that was recently discovered to be associated with the *Fermi Large Area Telescope* source 4FGL J1653.6–0158 (Nieder et al. 2020). The pulsar nature is confirmed by gamma-ray pulsations with Einstein@Home (Allen et al. 2013). Consistency in astrometry with *Gaia* has been confirmed by Nieder et al. (2020). We therefore also include this pulsar in our calculation.

PSR J2039–5617 is another pulsar confirmed by detection of gamma-ray pulsations (Clark et al. 2021), where a *Gaia* DR2 counterpart was confirmed. In our search, this counterpart is ≈8 mas from the Gaia DR3 source 6469722508861870080 and has consistent and better constrained astrometry compared to DR2. This match is therefore also robust.

[3]https://gitlab.com/icc-ub/public/gaiadr3_zeropoint

2.6 Radio inteferometric and timing astrometry

There are a few of XRBs and binary pulsars with literature astrometry measured by radio observations (interferometric or timing), which might be more constrained compared to *Gaia*. We adopt radio measurement in our analyses if *Gaia* astrometry is not available or if radio parallax or any of the proper motion component is more constrained than *Gaia* measurement.

Of the selected binaries, 14 have known radio parallaxes and/or proper motions, 10 of which have more constrained radio astrometry. These binaries are summarised in Table 1 and are indicated with superscripts that point to the corresponding references.

2.7 The final sample

The analysis in this work (Section 3.3) is built on 3D physical velocities, which in turn requires input of proper motion, systemic radial velocity (γ), and distance (or parallax). Therefore, from the list of binaries that have *Gaia* counterparts, we are specifically interested in those with already established γ, as well as

(i) well-constrained *Gaia* parallaxes (ϖ) such that $0 < \sigma_\varpi/\varpi < 0.2$, or
(ii) already constrained distances in literature.

Including the two BH-LMXBs that only have radio parallaxes and proper motions, i.e. GRS 1915+105 and MAXI J1836–194, our final sample contains a total of 89 binaries. There are four binaries that have known γ values but has no well-constrained parallaxes or established distances, including 2S 0921–630, GX 1+4, BW Cir, and GX 339–4. On the one hand, BW Cir and GX 339–4 have lower limits on $d_{\rm lit}$ (Table S1, available online), but the *Gaia* parallax of BW Cir corresponds to a closer distance $\approx 7.1^{+4.8}_{-3.9}$ kpc (see e.g. Gandhi et al. 2019; Plotkin et al. 2021). 2S 0921–630 and GX 1 + 4, on the other hand, only have approximate distances. These two sources are listed in Table S1 but are not used in modelling the distance prior (Section 2.8). All of these 89 sources are summarised in Table 1. Galactic distribution of these binaries are shown in Fig. S1 and S2 (available online).

2.8 The distances

We denote the distances estimated from trigonometric parallaxes by d_ϖ. For our estimation, we treat relatively nearby binaries ($\varpi > 2$) that have well-constrained ($\sigma_\varpi/\varpi < 0.2$) parallaxes separately from the other binaries. Since they have good-quality astrometric solution, we directly invert the parallax to get the distance, i.e. $d_\varpi = 1/\varpi$, and the uncertainty is simply propagated from the uncertainty in parallax, i.e. $\sigma_{d_\varpi} = \sigma_\varpi/\varpi^2$. For other binaries, we follow a Bayesian approach to infer distances from parallaxes.

2.8.1 *Pulsars*

Lorimer et al. (2006) derived a Galactic pulsar distribution in the vertical (z) and radial (r) directions (equations 10 and 11 of Lorimer et al. 2006). Based on the distributions, Verbiest et al. (2012) derived a distance prior for pulsars as:

$$p(\mathrm{d}|z, r) \propto \mathrm{d}^2 r^{1.9} \exp\left[-\frac{|z|}{E} - \frac{5(r - R_\odot)}{R_\odot}\right]. \quad (1)$$

Here, r is the Galactocentric distance projected in the Galactic plane, and z is the vertical coordinate in cylindrical Galactocentric frame, which are both implicitly dependent on d. E is the vertical scale

Table 1. Selected *Gaia* counterparts.

Name	Class	Gaia DR3	α (ICRS) (h:m:s)	δ (ICRS) ($^\circ:':''$)	ϖ (mas)	$\mu_\alpha \cos\delta$ (masyr^{-1})	μ_δ (masyr^{-1})
2S 0921–630	NS-LMXB	5 250 451 391 698 996 992	09:22:34.669	−63:17:41.288	0.10 ± 0.02	−3.16 ± 0.03	4.25 ± 0.03
4U 1254–69	NS-LMXB	5 844 938 121 765 636 864	12:57:37.167	−69:17:19.018	0.18 ± 0.16	−5.34 ± 0.19	−1.32 ± 0.21
Cen X-4	NS-LMXB	6 205 715 168 442 046 592	14:58:21.936	−31:40:08.406	0.55 ± 0.13	0.84 ± 0.15	−55.68 ± 0.13
Sco X-1	NS-LMXB	4 328 198 145 165 324 800	16:19:55.061	−15:38:25.215	0.47 ± 0.02	−7.19 ± 0.03	−12.33 ± 0.02
4U 1636–536	NS-LMXB	5 930 753 870 442 684 544	16:40:55.587	−53:45:05.081	0.29 ± 0.12	−5.90 ± 0.16	−8.33 ± 0.12
Her X-1	NS-LMXB	1 338 822 021 487 330 304	16:57:49.809	+35:20:32.361	0.14 ± 0.01	−1.21 ± 0.01	−7.86 ± 0.02
MXB 1659–298	NS-LMXB	6 029 391 608 332 996 224	17:02:06.534	−29:56:44.286	0.22 ± 0.23	−1.62 ± 0.52	−1.51 ± 0.33
4U 1700+24	NS-LMXB	4 571 810 378 118 789 760	17:06:34.503	+23:58:18.550	1.87 ± 0.05	−8.73 ± 0.04	−5.57 ± 0.05
GX 1+4	NS-LMXB	4 110 236 324 513 030 656	17:32:02.149	−24:44:44.161	−0.02 ± 0.07	−3.52 ± 0.08	−1.99 ± 0.06
4U 1735–444	NS-LMXB	5 955 379 701 104 735 104	17:38:58.233	−44:27:00.820	0.12 ± 0.10	−3.47 ± 0.12	−7.54 ± 0.07
XTE J1814–338	NS-LMXB	4 039 437 121 598 306 176	18:13:39.102	−33:46:23.865	1.07 ± 0.48	2.80 ± 0.47	−3.99 ± 0.40
2A 1822–371	NS-LMXB	6 728 016 172 687 965 568	18:25:46.806	−37:06:18.570	0.18 ± 0.03	−9.15 ± 0.04	−2.53 ± 0.03
Ser X-1	NS-LMXB	4 283 919 201 304 278 912	18:39:57.544	+05:02:09.433	−0.00 ± 0.27	−1.14 ± 0.36	−3.63 ± 0.27
Aql X-1	NS-LMXB	4 264 296 556 603 631 872	19:11:16.055	+00:35:05.786	0.21 ± 0.28	−1.80 ± 0.58	−5.13 ± 0.58
Cyg X-2	NS-LMXB	1 952 859 683 185 470 208	21:44:41.152	+38:19:17.061	0.10 ± 0.02	−1.79 ± 0.02	−0.32 ± 0.02
IGR J00370+6122	NS-HMXB	427 234 969 757 165 952	00:37:09.632	+61:21:36.479	0.29 ± 0.01	−1.80 ± 0.01	−0.53 ± 0.01
2S 0114+650	NS-HMXB	524 924 310 153 249 920	01:18:02.694	+65:17:29.841	0.22 ± 0.01	−1.24 ± 0.01	0.76 ± 0.01
RX J0146.9+6121	NS-HMXB	511 220 031 584 305 536	01:47:00.210	+61:21:23.662	0.37 ± 0.02	−1.03 ± 0.02	−0.08 ± 0.02
LS I +61 303	NS-HMXB	465 645 515 129 855 872	02:40:31.664	+61:13:45.590	0.40 ± 0.01	−0.42 ± 0.01	−0.26 ± 0.01
X Persi	NS-HMXB	168 450 545 792 009 600	03:55:23.076	+31:02:45.010	1.67 ± 0.04	−1.28 ± 0.05	−1.87 ± 0.03
XTE J0421+560	NS-HMXB	276 644 757 710 014 976	04:19:42.135	+55:59:57.698	0.24 ± 0.01	−0.47 ± 0.02	−0.51 ± 0.01
EXO 051910+3737.7	NS-HMXB	184 497 471 323 752 064	05:22:35.233	+37:40:33.575	0.76 ± 0.03	1.30 ± 0.04	−4.00 ± 0.03
1A 0535+262	NS-HMXB	3 441 207 615 229 815 040	05:38:54.574	+26:18:56.791	0.56 ± 0.02	−0.59 ± 0.03	−2.88 ± 0.02
HD 259 440	NS-HMXB	3 131 822 364 779 745 536	06:32:59.257	+05:48:01.154	0.57 ± 0.02	−0.03 ± 0.02	−0.43 ± 0.02
IGR J08408–4503	NS-HMXB	5 522 306 019 626 566 528	08:40:47.780	−45:03:30.138	0.45 ± 0.02	−7.46 ± 0.02	6.10 ± 0.02
Vela X-1	NS-HMXB	5 620 657 678 322 625 920	09:02:06.854	−40:33:16.751	0.51 ± 0.02	−4.82 ± 0.01	9.28 ± 0.02
2FGL J1019.0–5856	NS-HMXB	5 255 509 901 121 774 976	10:18:55.574	−58:56:45.939	0.23 ± 0.01	−6.45 ± 0.01	2.26 ± 0.01
Cen X-3	NS-HMXB	5 337 498 593 446 516 480	11:21:15.085	−60:37:25.593	0.15 ± 0.01	−3.12 ± 0.02	2.33 ± 0.01
1E 1145.1–6141	NS-HMXB	5 334 851 450 481 641 088	11:47:28.546	−61:57:13.389	0.12 ± 0.01	−6.23 ± 0.01	2.36 ± 0.01
2S 1145–619	NS-HMXB	5 334 823 859 608 495 104	11:48:00.007	−62:12:24.877	0.49 ± 0.02	−6.23 ± 0.02	1.60 ± 0.02
GX 301–2	NS-HMXB	6 054 569 565 614 460 800	12:26:37.548	−62:46:13.294	0.28 ± 0.02	−5.23 ± 0.02	−2.07 ± 0.02
1H 1253–761	NS-HMXB	5 837 600 152 935 767 680	12:39:14.458	−75:22:14.269	4.79 ± 0.03	−27.34 ± 0.03	−8.93 ± 0.04
1H 1249–637	NS-HMXB	6 055 103 928 246 312 960	12:42:50.236	−63:03:31.112	2.30 ± 0.08	−12.86 ± 0.07	−3.68 ± 0.07
1H 1255–567	NS-HMXB	6 060 547 335 455 660 032	12:54:36.828	−57:10:07.361	8.29 ± 0.12	−28.39 ± 0.09	−10.45 ± 0.11
4U 1538–52	NS-HMXB	5 886 085 557 746 480 000	15:42:23.352	−52:23:09.643	0.18 ± 0.02	−6.71 ± 0.01	−4.11 ± 0.01
4U 1700–37	NS-HMXB	5 976 382 915 813 535 232	17:03:56.776	−37:50:38.833	0.67 ± 0.03	2.41 ± 0.03	5.02 ± 0.02
IGR J17544–2619	NS-HMXB	4 063 908 810 076 415 872	17:54:25.272	−26:19:52.588	0.42 ± 0.03	−0.51 ± 0.03	−0.67 ± 0.02
LS 5039	NS-HMXB	4 104 196 427 943 626 624	18:26:15.064	−14:50:54.378	0.53 ± 0.02	7.43 ± 0.01	−8.15 ± 0.01
1H 2202+501	NS-HMXB	1 979 911 002 134 040 960	22:01:38.206	+50:10:04.629	0.90 ± 0.01	2.36 ± 0.01	−0.29 ± 0.01
4U 2206+543	NS-HMXB	2 005 653 524 280 214 400	22:07:56.229	+54:31:06.356	0.32 ± 0.01	−4.17 ± 0.02	−3.32 ± 0.01
A 0620–00	BH-LMXB	3 118 721 026 600 835 328	06:22:44.542	−00:20:44.373	0.73 ± 0.12	−0.44 ± 0.11	−5.14 ± 0.10
XTE J1118+480	BH-LMXB	789 430 249 033 567 744	11:18:10.764	+48:02:12.208	0.18 ± 0.27	−18.10 ± 0.16	−6.69 ± 0.22
GRS 1124–684	BH-LMXB	5 234 956 524 083 372 544	11:26:26.588	−68:40:32.900	0.19 ± 0.24	−2.93 ± 0.24	−1.39 ± 0.26
MAXI J1305–704	BH-LMXB	5 843 823 766 718 594 560	13:06:55.280	−70:27:05.101	−0.50 ± 0.57	−7.89 ± 0.62	−0.16 ± 0.72
BW Cir	BH-LMXB	5 852 296 053 620 905 472	13:58:09.710	−64:44:05.292	1.28 ± 0.53	−5.07 ± 0.63	−2.11 ± 0.58
4U 1543–475	BH-LMXB	5 986 117 923 045 619 072	15:47:08.265	−47:40:10.370	0.22 ± 0.06	−7.54 ± 0.05	−5.36 ± 0.05
XTE J1550–564	BH-LMXB	5 884 099 221 246 440 064	15:50:58.651	−56:28:35.314	2.29 ± 2.58	−6.49 ± 1.96	−3.49 ± 1.74
GRO 1655–40	BH-LMXB	5 969 790 961 312 131 456	16:54:00.136	−39:50:44.881	0.33 ± 0.05	−4.33 ± 0.06	−7.46 ± 0.05
GX 339–4	BH-LMXB	5 938 658 156 448 950 528	17:02:49.381	−48:47:23.166	0.21 ± 0.12	−3.95 ± 0.07[a]	−4.71 ± 0.06[a]
H 1705–250	BH-LMXB	4 112 450 294 268 643 456	17:08:14.500	−25:05:30.296	2.15 ± 1.67	−6.97 ± 2.83	−8.51 ± 1.38
Swift J1753.5–0127	BH-LMXB	4 178 766 135 477 201 408	17:53:28.291	−01:27:06.313	0.17 ± 0.09	0.99 ± 0.09	−3.54 ± 0.09
MAXI J1820+070	BH-LMXB	4 477 902 563 164 690 816	18:20:21.939	+07:11:07.184	0.40 ± 0.08	−3.09 ± 0.09	−6.29 ± 0.09
MAXI J1836–194	BH-LMXB	···	18:35:43.445[b]	−19:19:10.484[b]	···	−2.30 ± 0.60[c]	−6.10 ± 1.00[c]
GRS 1915+105	BH-LMXB	···	19:15:11.550[d]	+10:56:44.800[d]	···	−2.86 ± 0.07[e]	−6.20 ± 0.09[e]
V404 Cyg	BH-LMXB	2 056 188 624 872 569 088	20:24:03.818	+33:52:01.837	0.42 ± 0.02[f]	−5.18 ± 0.08	−7.78 ± 0.09
HD 96 670	BH-HMXB?	5 337 747 731 560 719 616	11:07:13.920	−59:52:23.153	0.32 ± 0.03	−6.75 ± 0.03	1.69 ± 0.03
V4641 Sgr	BH-HMXB	4 053 096 388 919 082 368	18:19:21.633	−25:24:25.843	0.21 ± 0.03	−0.78 ± 0.03	0.43 ± 0.02
SS 433	BH-HMXB?	4 293 406 612 283 985 024	19:11:49.562	+04:58:57.751	0.13 ± 0.02	−3.03 ± 0.02	−4.78 ± 0.02
Cyg X-1	BH-HMXB	2 059 383 668 236 814 720	19:58:21.671	+35:12:05.684	0.47 ± 0.01	−3.80 ± 0.01[g]	−6.28 ± 0.02[g]
MWC 656	BH-HMXB?	1 982 359 580 155 628 160	22:42:57.298	+44:43:18.209	0.51 ± 0.02	−3.48 ± 0.02	−3.16 ± 0.02
PSR J0348+0432	LM-PSR	3 273 288 485 744 249 344	03:48:43.640	+04:32:11.458	0.47 ± 0.47[h]	4.04 ± 0.16[h]	3.50 ± 0.60[h]
PSR J1012+5307	LM-PSR	851 610 861 391 010 944	10:12:33.439	+53:07:02.134	1.75 ± 0.29	2.64 ± 0.04[i]	−25.54 ± 0.04[i]
PSR J1023+0038	LM-PSR	3 831 382 647 922 429 952	10:23:47.689	+00:38:40.729	0.73 ± 0.02[j]	4.76 ± 0.03[j]	−17.34 ± 0.04[j]

Table 1 – *continued*

Name	Class	Gaia DR3	α (ICRS) (h:m:s)	δ (ICRS) ($^\circ:':''$)	ϖ (mas)	$\mu_\alpha \cos\delta$ (masyr^{-1})	μ_δ (masyr^{-1})
PSR J1024–0719	LM-PSR	3 775 277 872 387 310 208	10:24:38.661	−07:19:19.819	0.83 ± 0.13^k	-35.28 ± 0.01^k	-48.23 ± 0.03^k
PSR J1048+2339	LM-PSR	3 990 037 124 929 068 032	10:48:43.416	+23:39:53.392	0.50 ± 0.44	-15.45 ± 0.35	-11.62 ± 0.34
XSS J12270–4859	LM-PSR	6 128 369 984 328 414 336	12:27:58.717	−48:53:42.708	0.49 ± 0.13	-18.77 ± 0.11	7.30 ± 0.09
PSR B1259–63	HM-PSR	5 862 299 960 127 967 488	13:02:47.637	−63:50:08.632	0.46 ± 0.01	-7.09 ± 0.01	-0.34 ± 0.01
PSR J1306–4035	LM-PSR	6 140 785 016 794 586 752	13:06:56.272	−40:35:23.399	0.34 ± 0.15	-6.18 ± 0.14	4.16 ± 0.11
PSR J1311–3430	LM-PSR	6 179 115 508 262 195 200	13:11:45.721	−34:30:30.376	1.95 ± 0.97	-6.13 ± 1.60	-5.14 ± 0.68
PSR J1417–4402	LM-PSR	6 096 705 840 454 620 800	14:17:30.566	−44:02:57.580	0.24 ± 0.05	-4.76 ± 0.04	-5.10 ± 0.05
PSR J1431–4715	LM-PSR	6 098 156 298 150 016 768	14:31:44.613	−47:15:27.632	0.56 ± 0.13	-11.82 ± 0.14	-14.52 ± 0.15
PSR J1622–0315	LM-PSR	4 358 428 942 492 430 336	16:22:59.627	−03:15:37.266	0.64 ± 0.30	-13.18 ± 0.32	2.30 ± 0.23
PSR J1628–3205	LM-PSR	6 025 344 817 107 454 464	16:28:07.002	−32:05:49.021	0.69 ± 0.41	-6.19 ± 0.47	-21.43 ± 0.34
PSR J1653–0158	LM-PSR	4 379 227 476 242 700 928	16:53:38.053	−01:58:36.895	1.79 ± 0.78	-17.30 ± 0.95	-3.24 ± 0.72
PSR J1723–2837	LM-PSR	4 059 795 674 516 044 800	17:23:23.179	−28:37:57.595	1.11 ± 0.04	-11.73 ± 0.04	-24.05 ± 0.03
PSR J1816+4510	LM-PSR	2 115 337 192 179 377 792	18:16:35.934	+45:10:33.847	0.22 ± 0.10	5.30 ± 0.80^l	-3.00 ± 1.00^l
PSR J2039–5617	LM-PSR	6 469 722 508 861 870 080	20:39:34.968	−56:17:09.276	0.51 ± 0.17	3.86 ± 0.14	-15.18 ± 0.12
PSR J2129–0429	LM-PSR	2 672 030 065 446 134 656	21:29:45.060	−04:29:06.811	0.51 ± 0.07	12.10 ± 0.07	10.19 ± 0.06
PSR J2215+5135	LM-PSR	2 001 168 543 319 218 048	22:15:32.687	+51:35:36.437	0.32 ± 0.23	0.01 ± 0.24	2.24 ± 0.24
PSR J2339–0533	LM-PSR	2 440 660 623 886 405 504	23:39:38.745	−05:33:05.273	0.55 ± 0.18	3.92 ± 0.20	-10.28 ± 0.19
J05215658	BH-HMNI	207 628 584 632 757 632	05:21:56.591	+43:59:21.899	0.41 ± 0.02	-0.50 ± 0.02	-3.46 ± 0.01
J06163552	NS-LMNI	3 425 175 331 243 738 240	06:16:35.525	+23:19:09.285	0.96 ± 0.02	-1.43 ± 0.02	-4.97 ± 0.01
J112306.9	NS-LMNI	770 431 444 010 267 392	11:23:06.909	+40:07:36.366	3.19 ± 0.04	-20.60 ± 0.03	-24.28 ± 0.04
J125556.57	NS-LMNI	1 577 114 915 964 797 184	12:55:56.553	+56:58:46.498	1.73 ± 0.01	-9.12 ± 0.01	10.67 ± 0.01
Gaia BH2	BH-LMNI	5 870 569 352 746 779 008	13:50:16.732	−59:14:20.418	0.86 ± 0.02	-10.48 ± 0.10	-4.61 ± 0.06
J15274848	NS-LMNI	1 375 051 479 376 039 040	15:27:48.437	+35:36:57.376	8.48 ± 0.01	-32.00 ± 0.01	4.07 ± 0.01
Gaia BH1	BH-LMNI	4 373 465 352 415 301 632	17:28:41.090	−00:34:51.931	2.10 ± 0.02	-7.70 ± 0.02	-25.85 ± 0.03
AS 386	BH-HMNI	2 061 686 870 220 386 816	20:10:54.197	+38:18:09.284	0.17 ± 0.01	-2.66 ± 0.01	-4.88 ± 0.01
J235456.76	NS-LMNI	2 874 966 759 081 257 728	23:54:56.765	+33:56:25.697	7.86 ± 0.02	23.21 ± 0.02	-18.93 ± 0.01

ϖ is the parallax after zero-point correction except for Gaia BH1 and BH2.
Classes: (NS)BH−(H)LMXB: (NS) BH (high) LM XRB; (NS)BH−(H)LMNI: NI NS (BH).
Binary with a (high) LM companions; (H)LM-PSR: binary pulsar with a (high) LM companion.
References: [a]: Atri et al. (2019), [b]: Russell et al. (2015), [c]: Russell et al. (2014), [d]: Dhawan, Mirabel & Rodríguez (2000), [e]: Reid et al. (2014b), [f]: Miller-Jones et al. (2009), [g]: Miller-Jones et al. (2021), [h]: Antoniadis et al. (2013), [i]: ATNF, [j]: Deller et al. (2012), [k]: Reardon et al. (2021), and [l]: Stovall et al. (2014).

height, for which we choose $E = 500$ pc as suggested by Verbiest et al. (2012).

We use a Gaussian likelihood (see e.g. Bailer-Jones et al. 2021) that centres on the inverse of the distance and spreads according to the uncertainty on parallax, i.e.:

$$p(\varpi|\mathrm{d}, \sigma_\varpi) = \frac{1}{\sqrt{2\pi}\sigma_\varpi} \exp\left[-\frac{1}{2\sigma_\varpi^2}\left(\varpi - \frac{1}{d}\right)^2\right], \quad (2)$$

where the ϖ and σ_ϖ are parallax and the associated uncertainty, respectively. The posterior of distance is then given by Bayes' theorem:

$$p(\mathrm{d}|\varpi, \sigma_\varpi, z, r) \propto p(\mathrm{d}|z, r)p(\varpi|\mathrm{d}, \sigma_\varpi). \quad (3)$$

2.8.2 *XRBs and others*

The remaining binaries are primarily XRBs and several NI binaries that likely host a BH or NS. To make a probabilistic estimate of their distances, we use the same likelihood as that for the pulsars [equation (2)], and the exponential prior following Gandhi et al. (2019), which has the form of:

$$p(\mathrm{d}) = \begin{cases} \frac{1}{2L^3}\mathrm{d}^2 \exp\left(-\frac{\mathrm{d}}{L}\right) & r > 0 \\ 0 & r \leq 0 \end{cases}. \quad (4)$$

This prior is characterised only by a scaling parameter L, which was found to be 2.17 ± 0.12 kpc by Gandhi et al. (2019).

In this work, we use a more extended sample to model this prior. Since this prior is used for XRBs and NI binaries with compact objects, we cross-check the list of sources in L06, L07, and BlackCAT for distances not inferred from parallaxes (denoted by $d_{\rm lit}$), including only values of $d_{\rm lit}$ that have reported uncertainties or lower limits. The final $d_{\rm lit}$ sample includes a total of 125 such binaries, which are summarised in Table S1. Most of the constrained values of $d_{\rm lit}$ have symmetric uncertainties, while for the asymmetric uncertainties, we use the central value ($(d_{\rm lit,\,low} + d_{\rm lit,\,up})/2$) for our modelling. For the constrained values, we draw 10 000 random distances for each binary in the sample as per a Gaussian distribution, with the standard deviation set to the maximum between upper and lower uncertainties; for the lower limits on $d_{\rm lit}$, we sample from a flat distribution between $d_{\rm lit,\,low}$ and $d_{\rm lit,\,low} + 5$ kpc – this upper limit was used by Gandhi et al. (2019) who also found that the result is not sensitive on choices of this limit. For each set of random distances, we compute the joint probability

$$\mathcal{L}_n = \prod_i p(d_{i,n}|L), \quad (5)$$

where p is given by equation (4), i indicates binaries in the sample, and n indexes the random realisations. We search on a grid of L for the value that maximises the joint probability – considered a best-fitting scaling parameter. This procedure results in a distribution of L with a median of $1.97^{+0.05}_{-0.05}$ kpc (errors correspond to 16th and 84th percentiles).

With the constructed likelihood and priors, we make Bayesian distance inference for binaries with good astrometry ($\sigma_\varpi/\varpi < 0.2$)

Table 2. Galactic and solar constants used in this work.

Name	Value	Unit	Ref	Description
E	0.5	kpc	[1]	Galactic scale height of pulsar distribution; used in equation (1)
L	1.97 ± 0.05	kpc	[2]	Scaling parameter of the distance prior in equation (4)
$R_\odot$	8.34 ± 0.16	kpc	[3]	Galactocentric solar distance projected onto the plane
$\Theta_\odot$	240 ± 8	kms^{-1}	[3]	Galactic rotation velocity at the location of the Sun
$U_\odot$	10.7 ± 1.8	kms^{-1}	[3]	
$V_\odot$	15.6 ± 6.8	kms^{-1}	[3]	Cartesian components of solar motion relative to the local standard of rest
$W_\odot$	8.9 ± 0.9	kms^{-1}	[3]	

References: [1] Verbiest et al. (2012), [2] This work, and [3] Reid et al. (2014a).

and sample a total of 10^6 random distances as per their posterior distributions using inverse transform sampling. In Table 3, we report medians and calculating a 68.27 per cent equal-tailed interval of the sampled distances for each binary.

2.9 The peculiar velocities

Peculiar velocity ($v_{\rm pec}$) is the magnitude of 3D velocity relative to local Galactic rotation. For our calculation, we want to propagate uncertainties not only in source-specific parameters (parallax, proper motion, and radial velocity) but also in Galactic constants (Table 2) to the final $v_{\rm pec}$; we therefore follow the formulation derived by Reid et al. (2009), assuming a Gaussian distribution for the source kinematic parameters, viz. proper motion and radial velocity, and for the Galactic constants. Distances are sampled from the posterior derived in Section 2.8; for binaries that have poorly constrained or invalid (zero or negative) *Gaia* parallaxes (Section 2.7), we sample from a Gaussian distribution that centres at the distances inferred from dispersion measures from Yao et al. (2017) with 20 per cent uncertainty as standard deviation for pulsars, and a Gaussian distribution that centres at the $d_{\rm lit}$ with symmetrised (averaged upper and lower error) uncertainty for the others (Table S1). In the last step of the calculation, the local Galactic rotation needs to be subtracted (Reid et al. 2009) from the Galactocentric 3D velocity; for this, we adjust the MWPotential2014 potential in the GALPY package[4] (version 1.8.3, Bovy 2015) to adopt the Galactic constants used in this work (Table 2) and use it to find the local rotation velocity.

As mentioned in Section 2.7, there are four binaries that have neither well-constrained *Gaia* parallaxes nor $d_{\rm lit}$, but two of them have lower limits on $d_{\rm lit}$ ($d_{\rm lit,\,low}$), i.e. BW Cir and GX 339–4; for these two binaries, we sample from the same distribution as that in modelling the exponential prior (Section 2.8), i.e. a uniform distribution between $d_{\rm lit,\,low}$ and $d_{\rm lit,\,low} + 5$ kpc, while for the other two, we sample from a Gaussian distribution that centres at the nominal $d_{\rm lit}$ with a 20 per cent uncertainty. $v_{\rm pec}$ is calculated for these four binaries but should be treated with care. Indeed, physical velocities have a non-negligible dependence on distances; these four binaries are therefore not included in further statistical analyses.

With all the randomised parameters, we compute a sample of 10^6 $v_{\rm pec}$ values for each binary. Because the calculation uses present-day astrometric parameters, we refer to the calculated $v_{\rm pec}$ as present-day peculiar velocity, denoted by $v_{\rm pec,\,p}$. We report median values and errors corresponding to 16th and 84th percentiles of $v_{\rm pec,\,p}$ in Table 3.

[4] http://github.com/jobovy/galpy

2.10 Potential peculiar velocity at birth

The calculated $v_{\rm pec,\,p}$ could deviate from the $v_{\rm pec}$ at birth depending on the binary's position and kinematics under the influence of Galactic potential. We therefore also calculate the potential birth peculiar velocities (denoted by $v_{\rm pec}^{z=0}$) following the methods used by Atri et al. (2019), who referred to these as 'potential kick velocities'. In short, for each binary, we set up a total of 5000 orbit instances by randomly drawing proper motions and γ values from a Gaussian and distances from the posteriors calculated in Section 2.8. We then integrate these orbits of the binaries backward in time for 10 Gyr using GALPY and record the $v_{\rm pec}$ values every time the binary passes the Galactic plane (i.e. at $z = 0$). The plane crossing epochs are found by linearly interpolating the $z(t)$ component of the orbit near the Galactic plane, which are then fed to the time-dependent $v_{\rm pec}$ functions to obtain the $v_{\rm pec}^{z=0}$ distributions. The resulting $v_{\rm pec}^{z=0}$ are the potential $v_{\rm pec}$ values at birth under the assumption that the binaries are born in the Galactic plane. Similar to $v_{\rm pec,\,p}$, the $v_{\rm pec}^{z=0}$s and the errors corresponding to 16th and 84th percentiles are summarized in Table 3, and $v_{\rm pec}^{z=0}$ distributions are shown in Fig. S1–S4 (available online).

Given the same uncertainties in all other parameters, $v_{\rm pec}^{z=0}$ involves time as an extra variable that could complicate the final distributions over $v_{\rm pec,\,p}$. However, calculation of $v_{\rm pec}^{z=0}$ also reduces possible effects of time by bringing all binaries to the same epoch (the birth time) of their evolution. Moreover, $v_{\rm pec}^{z=0}$ relates to the epoch near the birth, while using $v_{\rm pec,\,p}$ as the proxy could underestimate the effect of binary evolution on the kinematics (e.g. mass loss due to stellar winds, unconservative mass transfer, etc.).

Our statistical analyses (Sections 3.2–3.5) are performed on $v_{\rm pec}^{z=0}$ and $v_{\rm pec,\,p}$, but in this paper, we only report results obtained with $v_{\rm pec}^{z=0}$. Because $v_{\rm pec,\,p}$ are generally consistent with $v_{\rm pec}^{z=0}$ at 68 per cent confidence level (Fig. 1), results using $v_{\rm pec,\,p}$ are in agreement with those using $v_{\rm pec}^{z=0}$.

3 ANALYSIS AND RESULTS

3.1 Comparing with literature distances

Distances are clearly crucial in interpreting our peculiar velocities, and so we compare the well-constrained parallax-inferred distances (d_ϖ; Section 2.7), with values in the literature ($d_{\rm lit}$; Table S1) if available. In Fig. 2, we can see that d_ϖ agrees with $d_{\rm lit}$ for most binaries. However, there are two clear outliers, 2A 1822−371 and AS 386, that have somewhat smaller $d_{\rm lit}$, despite both sources having an acceptable *Gaia* Renormalized Unit Weight Error (`ruwe`) value of

Table 3. Binary properties: (1) Name. (2) Class. (3) Systemic radial velocity. (4) Distance (used in calculation). (5) Present-day peculiar velocity. (6) Potential peculiar velocity at birth. (7) Compact object mass. (8) Mass of non-degenerate companion. (9) Orbital period.

Name	Class	γ ($\mathrm{km\,s^{-1}}$)	d (kpc)	$v_{\mathrm{pec,\,p}}$ ($\mathrm{km\,s^{-1}}$)	$v_{\mathrm{pec}}^{z=0}$ ($\mathrm{km\,s^{-1}}$)	M_1 ($\mathrm{M_\odot}$)	M_2 ($\mathrm{M_\odot}$)	P_{orb} (d)
(1)	(2)	(3)	(4)	(5)	(6)	(7)	(8)	(9)
2S 0921−630	NS-LMXB	44.4 ± 2.4 [1]	8.5*	$38.2^{+18.6}_{-7.4}$	$58.9^{+10.4}_{-3.9}$	$1.4^{+0.1}_{-0.1}$ [2]	$0.3^{+0.0}_{-0.0}$ [2]	9.00 [3]
4U 1254−69	NS-LMXB	183.0 ± 3.0 [4]	$13.0^{+3.0\dagger}_{-3.0}$	$155.3^{+29.0}_{-17.6}$	$202.9^{+81.1}_{-52.9}$	$1.5^{+0.3}_{-0.3}$ [4]	$0.5^{+0.1}_{-0.1}$ [4]	0.16 [5]
Cen X-4	NS-LMXB	194.5 ± 0.2 [6]	$1.4^{+0.3\dagger}_{-0.3}$	$418.7^{+72.1}_{-68.5}$	$457.2^{+84.1}_{-137.8}$	$1.9^{+0.4}_{-0.8}$ [6]	$0.3^{+0.2}_{-0.1}$ [6]	0.63 [6]
Sco X-1	NS-LMXB	−113.8 ± 0.6 [7]	$2.2^{+0.1}_{-0.1}$	$167.5^{+10.3}_{-9.8}$	$210.6^{+19.0}_{-29.0}$	1.4*	0.4* [8]	0.79 [9]
4U 1636−536	NS-LMXB	−34.0 ± 5.0 [10]	$6.0^{+0.5\dagger}_{-0.5}$	$164.7^{+12.6}_{-12.6}$	$194.6^{+15.0}_{-25.7}$	1.4*	0.5* [10]	0.16 [10]
Her X-1	NS-LMXB	−65.0 ± 2.0 [11]	$7.1^{+0.8}_{-0.6}$	$125.5^{+11.3}_{-10.9}$	$198.5^{+13.2}_{-32.0}$	$1.5^{+0.3}_{-0.3}$ [11]	$2.3^{+0.3}_{-0.3}$ [11]	1.70 [11]
MXB 1659−298	NS-LMXB	−49.0 ± 16.0 [12]	$9.0^{+2.0\dagger}_{-2.0}$	$259.7^{+92.1}_{-203.6}$	$271.4^{+116.9}_{-149.3}$	$2.1^{+0.9}_{-0.9}$ [12]	$0.6^{+0.2}_{-0.2}$ [12]	0.30 [13]
4U 1700+24	NS-LMXB	−47.4 ± 0.1 [14]	$0.5^{+0.0}_{-0.0}$	$39.2^{+9.5}_{-8.8}$	$56.7^{+6.3}_{-7.5}$	1.4*	$1.6^{+0.1}_{-0.2}$ [14]	4391.00 [14]
GX 1+4	NS-LMXB	−176.7 ± 0.2 [15]	4.3*	$189.3^{+8.1}_{-8.3}$	$186.3^{+15.2}_{-31.8}$	1.4*	<1.2 [15]	1160.80 [15]
4U 1735−444	NS-LMXB	−140.0 ± 3.0 [10]	$8.5^{+1.3\dagger}_{-1.3}$	$60.0^{+62.1}_{-30.7}$	$147.9^{+22.7}_{-19.7}$	1.4*	0.5* [10]	0.19 [10]
XTE J1814−338	NS-LMXB	−30.0 ± 20.0 [16]	$8.0^{+1.6\dagger}_{-1.6}$	$171.3^{+194.8}_{-51.1}$	$217.3^{+134.3}_{-73.2}$	$2.0^{+0.7}_{-0.5}$ [16]	$0.2^{+0.1}_{-0.1}$ [16]	0.18 [16]
2A 1822−371	NS-LMXB	−44.0 ± 5.0 [17]	$5.9^{+1.3}_{-0.9}$	$253.7^{+36.2}_{-33.2}$	$261.3^{+48.3}_{-36.4}$	$2.0^{+0.4}_{-0.4}$ [18]	$0.5^{+0.1}_{-0.1}$ [18]	0.23 [19]
Ser X-1	NS-LMXB	92.0 ± 4.0 [4]	$7.7^{+0.9\dagger}_{-0.9}$	$110.0^{+30.2}_{-31.3}$	$108.4^{+25.7}_{-22.3}$	1.4*	0.1* [4]	0.09 [4]
Aql X-1	NS-LMXB	104.0 ± 3.0 [20]	$5.2^{+0.8\dagger}_{-0.8}$	$42.3^{+13.2}_{-12.0}$	$55.5^{+7.8}_{-5.9}$	1.4*	<0.8 [20]	0.79 [20]
Cyg X-2	NS-LMXB	−207.8 ± 0.3 [21]	$9.7^{+1.9}_{-1.4}$	$164.0^{+9.0}_{-8.5}$	$240.0^{+23.5}_{-48.1}$	$1.7^{+0.2}_{-0.2}$ [21]	$0.6^{+0.1}_{-0.1}$ [21]	9.84 [21]
IGR J00370+6122	NS-HMXB	−77.3 ± 1.4 [22]	$3.4^{+0.1}_{-0.1}$	$23.4^{+9.7}_{-8.1}$	$29.4^{+5.3}_{-5.3}$	1.4*	$10.0^{+5.0}_{-5.0}$ [22]	15.66 [23]
2S 0114+650	NS-HMXB	−58.2 ± 0.5 [24]	$4.5^{+0.2}_{-0.2}$	$22.4^{+4.4}_{-2.2}$	$21.6^{+1.9}_{-2.4}$	1.4*	$16.0^{+5.0}_{-5.0}$ [25]	11.59 [26]
RX J0146.9+6121	NS-HMXB	−37.0 ± 4.3 [27]	$2.8^{+0.2}_{-0.2}$	$11.8^{+7.9}_{-4.2}$	$7.1^{+3.6}_{-2.4}$	1.4*	$11.0^{+2.0}_{-2.0}$ [28]	330.00* [27]
LS I +61 303	NS-HMXB	−41.4 ± 0.6 [29]	$2.5^{+0.1}_{-0.1}$	$9.0^{+7.0}_{-3.6}$	$9.1^{+2.3}_{-2.7}$	1.4*	$12.5^{+2.5}_{-2.5}$ [30]	24.50 [31]
X Persi	NS-HMXB	1.0 ± 0.9 [32]	$0.6^{+0.0}_{-0.0}$	$17.9^{+9.8}_{-7.8}$	$20.2^{+3.4}_{-3.0}$	1.4*	$14.0^{+3.0}_{-3.0}$ [32]	250.30 [33]
XTE J0421+560	NS-HMXB	−51.0 ± 2.0 [34]	$4.1^{+0.3}_{-0.2}$	$18.1^{+4.6}_{-3.2}$	$21.1^{+2.3}_{-2.5}$	1.4*	...	19.41 [34]
EXO 051910+3737.7	NS-HMXB	−20.5 ± 4.4 [35]	$1.3^{+0.1}_{-0.1}$	$24.4^{+6.4}_{-5.5}$	$23.8^{+5.4}_{-5.0}$	1.4*	...	...
1A 0535+262	NS-HMXB	−30.0 ± 4.0 [36]	$1.8^{+0.1}_{-0.1}$	$44.9^{+4.6}_{-4.5}$	$37.5^{+6.7}_{-6.5}$	$1.6^{+0.6}_{-0.6}$ [36]	$7.5^{+2.5}_{-2.5}$ [36]	111.00 [37]
HD 259 440	NS-HMXB	36.9 ± 0.8 [38]	$1.8^{+0.1}_{-0.1}$	$10.4^{+6.4}_{-2.9}$	$6.5^{+1.6}_{-2.1}$	1.4*	$16.1^{+2.9}_{-2.9}$ [39]	308.00* [38]
IGR J08408−4503	NS-HMXB	15.3 ± 0.5 [40]	$2.2^{+0.1}_{-0.1}$	$38.9^{+6.8}_{-5.1}$	$38.8^{+6.1}_{-6.1}$	1.4*	33.0* [40]	9.54 [40]
Vela X-1	NS-HMXB	−3.4 ± 1.0 [41]	$2.0^{+0.1}_{-0.1}$	$59.0^{+7.7}_{-6.8}$	$62.1^{+7.9}_{-8.8}$	$2.1^{+0.2}_{-0.2}$ [42]	$26.0^{+1.0}_{-1.0}$ [42]	8.96 [41]
2FGL J1019.0−5856	NS-HMXB	30.4 ± 1.3 [43]	$4.3^{+0.2}_{-0.2}$	$30.9^{+6.0}_{-3.4}$	$36.4^{+3.2}_{-3.0}$	1.4*	23.2* [44]	16.54 [45]
Cen X-3	NS-HMXB	39.0 ± 3.0 [46]	$6.9^{+0.7}_{-0.6}$	$102.4^{+4.2}_{-3.9}$	$108.5^{+11.2}_{-14.6}$	$1.6^{+0.1}_{-0.1}$ [42]	$24.0^{+1.0}_{-1.0}$ [42]	2.09* [47]
1E 1145.1−6141	NS-HMXB	−13.0 ± 3.0 [48]	$8.3^{+0.8}_{-0.6}$	$56.5^{+13.2}_{-10.2}$	$54.7^{+15.3}_{-11.3}$	$1.7^{+0.3}_{-0.3}$ [48]	$14.0^{+4.0}_{-4.0}$ [48]	14.37 [49]
2S 1145−619	NS-HMXB	−17.0 ± 7.4 [50]	$2.1^{+0.1}_{-0.1}$	$16.2^{+8.4}_{-4.3}$	$12.9^{+5.1}_{-3.0}$	1.4*	$13.0^{+2.0}_{-2.0}$ [51]	187.50* [47]
GX 301−2	NS-HMXB	4.1 ± 2.4 [52]	$3.6^{+0.2}_{-0.2}$	$58.0^{+4.7}_{-4.3}$	$59.8^{+6.7}_{-6.5}$	$1.9^{+0.6}_{-0.6}$ [52]	$43.0^{+10.0}_{-10.0}$ [52]	41.50 [52]
1H 1253−761	NS-HMXB	−20.0 ± 7.4 [50]	$0.2^{+0.0}_{-0.0}$	$27.5^{+10.9}_{-9.0}$	$26.2^{+9.3}_{-8.3}$	1.4*	7.5* [53]	...
1H 1249−637	NS-HMXB	22.0 ± 7.0 [50]	$0.4^{+0.0}_{-0.0}$	$21.0^{+11.5}_{-9.3}$	$28.6^{+9.9}_{-9.0}$	1.4*	...	...
1H 1255−567	NS-HMXB	13.0 ± 3.7 [50]	$0.1^{+0.0}_{-0.0}$	$12.5^{+7.0}_{-3.9}$	$14.4^{+5.0}_{-4.6}$	1.4*	...	...
4U 1538−52	NS-HMXB	−148.1 ± 0.9 [54]	$5.7^{+0.5}_{-0.5}$	$77.5^{+9.2}_{-10.0}$	$73.9^{+8.6}_{-8.5}$	$1.0^{+0.2}_{-0.2}$ [42]	$16.0^{+2.0}_{-2.0}$ [42]	3.71 [55]
4U 1700−37	NS-HMXB	−60.0 ± 12.0 [56]	$1.5^{+0.1}_{-0.1}$	$71.3^{+11.7}_{-11.5}$	$76.7^{+12.8}_{-13.4}$	$2.0^{+0.2}_{-0.2}$ [42]	$46.0^{+5.0}_{-5.0}$ [42]	3.41 [57]
IGR J17544−2619	NS-HMXB	−46.8 ± 4.0 [58]	$2.4^{+0.2}_{-0.1}$	$43.7^{+4.6}_{-4.4}$	$36.6^{+6.0}_{-5.6}$	1.4*	$23.0^{+2.0}_{-2.0}$ [59]	12.17 [58]
LS 5039	NS-HMXB	17.2 ± 0.7 [30]	$1.9^{+0.1}_{-0.1}$	$88.2^{+3.7}_{-3.2}$	$84.5^{+4.7}_{-4.1}$	$3.7^{+1.3}_{-1.0}$ [30]	$22.9^{+3.4}_{-2.9}$ [30]	3.91 [30]
1H 2202+501	NS-HMXB	−16.8 ± 2.5 [60]	$1.1^{+0.0}_{-0.0}$	$28.7^{+3.2}_{-2.5}$	$24.3^{+4.5}_{-4.3}$	1.4*	...	...
4U 2206+543	NS-HMXB	−61.5 ± 1.6 [61]	$3.1^{+0.1}_{-0.1}$	$27.8^{+6.6}_{-4.1}$	$26.3^{+5.3}_{-4.7}$	1.4*	$23.5^{+14.5}_{-8.0}$ [61]	9.55 [61]
A 0620−00	BH-LMXB	8.5 ± 1.8 [62]	$1.5^{+0.3}_{-0.2}$	$43.7^{+9.9}_{-7.1}$	$41.8^{+11.2}_{-8.6}$	$6.6^{+0.3}_{-0.3}$ [63]	$0.5^{+0.1}_{-0.1}$ [63]	0.32 [64]

Table 3 – *continued*

Name	Class	γ (kms^{-1})	d (kpc)	$v_{\rm pec,\,p}$ (kms^{-1})	$v_{\rm pec}^{z=0}$ (kms^{-1})	M_1 (M$_\odot$)	M_2 (M$_\odot$)	$P_{\rm orb}$ (d)
(1)	(2)	(3)	(4)	(5)	(6)	(7)	(8)	(9)
XTE J1118+480	BH-LMXB	2.7 ± 1.1 [65]	$1.7^{+0.1\dagger}_{-0.1}$	$142.9^{+11.4}_{-11.2}$	$172.0^{+18.9}_{-28.4}$	$7.5^{+0.7}_{-0.6}$ [66]	$0.2^{+0.1}_{-0.1}$ [66]	0.17 [64]
GRS 1124−684	BH-LMXB	14.2 ± 6.3 [67]	$5.0^{+0.7\dagger}_{-0.7}$	$118.6^{+15.5}_{-15.2}$	$115.1^{+19.3}_{-18.5}$	$11.0^{+2.1}_{-1.4}$ [68]	$0.9^{+0.2}_{-0.1}$ [68]	0.43 [69]
MAXI J1305−704	BH-LMXB	-9.0 ± 5.0 [70]	$7.7^{+1.6\dagger}_{-1.6}$	$58.1^{+30.4}_{-22.1}$	$75.1^{+17.4}_{-10.0}$	$8.9^{+1.6}_{-1.0}$ [70]	$0.4^{+0.2}_{-0.2}$ [70]	0.40 [70]
BW Cir	BH-LMXB	102.0 ± 4.0 [71]	$\geq$25.0	$352.0^{+106.9}_{-98.8}$	$279.3^{+156.9}_{-111.3}$	>7.6 [72]	>0.9 [72]	2.54 [72]
4U 1543−475	BH-LMXB	-87.0 ± 3.0 [73]	$7.5^{+0.5\dagger}_{-0.5}$	$99.0^{+14.5}_{-15.1}$	$118.7^{+11.1}_{-9.1}$	$9.4^{+1.0}_{-1.0}$ [74]	$2.6^{+0.6}_{-0.5}$ [74]	1.12 [74]
XTE J1550−564	BH-LMXB	-68.0 ± 19.0 [75]	$4.5^{+0.5\dagger}_{-0.5}$	$79.1^{+38.2}_{-32.3}$	$78.8^{+37.1}_{-30.4}$	$11.7^{+3.9}_{-3.9}$ [76]	$0.3^{+0.1}_{-0.1}$ [76]	1.54 [76]
GRO 1655−40	BH-LMXB	-167.1 ± 0.6 [77]	$3.2^{+0.6}_{-0.4}$	$161.8^{+7.4}_{-5.7}$	$153.6^{+13.9}_{-28.9}$	$6.0^{+0.4}_{-0.4}$ [78]	$2.5^{+0.3}_{-0.3}$ [78]	2.62 [79]
GX 339−4	BH-LMXB	26.0 ± 2.0 [80]	$\geq$5.0	$165.8^{+10.7}_{-34.7}$	$201.0^{+33.0}_{-37.2}$	$5.9^{+3.6}_{-3.6}$ [80]	$1.1^{+1.7}_{-0.8}$ [80]	1.76 [80]
H 1705−250	BH-LMXB	-54.0 ± 15.0 [81]	$8.6^{+2.1\dagger}_{-2.1}$	$221.2^{+100.8}_{-109.0}$	$289.4^{+71.3}_{-75.9}$	$6.4^{+1.5}_{-1.5}$ [81]	$0.3^{+0.1}_{-0.1}$ [81]	0.52 [82]
Swift J1753.5−0127	BH-LMXB	6.0 ± 6.0 [83]	$6.0^{+2.0\dagger}_{-2.0}$	$110.4^{+81.4}_{-57.1}$	$149.5^{+68.2}_{-59.6}$	>7.4 [84]	0.5* [84]	0.14 [85]
MAXI J1820+070	BH-LMXB	-21.6 ± 2.3 [86]	$2.8^{+0.8}_{-0.5}$	$72.4^{+18.7}_{-16.2}$	$105.4^{+24.6}_{-19.4}$	$8.4^{+0.8}_{-0.7}$ [87]	$0.6^{+0.1}_{-0.1}$ [87]	0.69 [86]
MAXI J1836−194	BH-LMXB?	61.0 ± 15.0 [88]	$7.0^{+3.0}_{-3.0}$	$98.4^{+32.2}_{-25.7}$	$133.4^{+32.1}_{-29.8}$	...	...	...
GRS 1915+105	BH-LMXB	12.3 ± 1.0 [89]	$8.6^{+2.0}_{-2.0}$	$31.8^{+17.5}_{-14.6}$	$39.6^{+19.6}_{-19.5}$	$12.4^{+2.0}_{-1.8}$ [89]	$0.5^{+0.4}_{-0.3}$ [89]	33.83 [90]
V404 Cyg	BH-LMXB	-0.4 ± 2.2 [91]	$2.4^{+0.1}_{-0.1}$	$45.3^{+3.9}_{-3.5}$	$38.7^{+5.7}_{-5.9}$	$9.0^{+0.2}_{-0.6}$ [92]	$0.6^{+0.1}_{-0.1}$ [92]	6.47 [93]
HD 96 670	BH-HMXB?	-27.5 ± 0.0 [94]	$3.1^{+0.3}_{-0.3}$	$24.3^{+10.0}_{-9.2}$	$25.6^{+4.4}_{-4.3}$	$6.2^{+0.9}_{-0.7}$ [94]	$22.7^{+5.2}_{-3.6}$ [94]	5.28 [94]
V4641 Sgr	BH-HMXB	107.4 ± 2.9 [76]	$4.8^{+0.7}_{-0.5}$	$91.8^{+6.6}_{-6.7}$	$101.4^{+10.1}_{-10.3}$	$6.4^{+0.6}_{-0.6}$ [95]	$2.9^{+0.4}_{-0.4}$ [95]	2.82 [96]
SS 433	BH-HMXB?	69.0 ± 4.7 [97]	$7.4^{+1.4}_{-1.1}$	$44.3^{+22.2}_{-15.9}$	$45.3^{+14.4}_{-12.0}$	$4.3^{+0.4}_{-0.4}$ [97]	$11.3^{+0.6}_{-0.6}$ [97]	13.08* [98]
Cyg X-1	BH-HMXB	-5.1 ± 0.5 [99]	$2.1^{+0.1}_{-0.1}$	$22.3^{+4.6}_{-2.9}$	$21.9^{+3.2}_{-3.0}$	$21.2^{+2.2}_{-2.2}$ [100]	$40.6^{+7.7}_{-7.1}$ [100]	5.60 [101]
MWC 656	BH-HMXB?	-2.8 ± 9.4 [102]	$2.0^{+0.1}_{-0.1}$	$25.8^{+13.7}_{-12.9}$	$36.2^{+9.7}_{-7.0}$	$4.1^{+1.4}_{-1.4}$ [102]	$7.8^{+2.0}_{-2.0}$ [103]	60.37 [103]
PSR J0348+0432	LM-PSR	-1.0 ± 20.0 [104]	$2.1^{+0.4\dagger}_{-0.4}$	$62.3^{+13.4}_{-12.3}$	$73.1^{+13.0}_{-11.4}$	$2.0^{+0.0}_{-0.0}$ [104]	$0.2^{+0.0}_{-0.0}$ [104]	0.10 [104]
PSR J1012+5307	LM-PSR	44.0 ± 8.0 [105]	$0.6^{+0.1}_{-0.1}$	$84.2^{+15.7}_{-11.9}$	$96.4^{+21.5}_{-14.7}$	$1.6^{+0.2}_{-0.2}$ [105]	$0.2^{+0.0}_{-0.0}$ [105]	0.60 [106]
PSR J1023+0038	LM-PSR	1.0 ± 3.0 [107]	$1.4^{+0.0}_{-0.0}$	$131.1^{+6.7}_{-6.3}$	$149.0^{+15.1}_{-25.3}$	$1.6^{+0.2}_{-0.2}$ [108]	$0.2^{+0.0}_{-0.0}$ [108]	0.20 [109]
PSR J1024−0719	LM-PSR	185.0 ± 4.0 [110]	$1.2^{+0.2}_{-0.2}$	$382.2^{+64.7}_{-45.8}$	$465.7^{+68.7}_{-84.7}$	1.4*	0.4* [111]	...
PSR J1048+2339	LM-PSR	-24.0 ± 8.0 [108]	$2.0^{+0.4\dagger}_{-0.4}$	$157.7^{+35.8}_{-35.4}$	$199.4^{+49.7}_{-46.0}$	>2.0 [108]	>0.4 [108]	0.25 [112]
XSS J12270−4859	LM-PSR	67.0 ± 2.0 [113]	$1.6^{+0.3\dagger}_{-0.3}$	$131.4^{+21.1}_{-20.8}$	$153.0^{+23.4}_{-24.5}$	1.4*	>0.3 [108]	0.29 [113]
PSR B1259−63	HM-PSR	0.0 ± 0.0 [114]	$2.2^{+0.1}_{-0.1}$	$24.8^{+9.4}_{-8.0}$	$34.4^{+4.9}_{-5.0}$	1.4*	23.0* [114]	1236.72 [114]
PSR J1306−4035	LM-PSR	32.0 ± 1.8 [115]	$4.7^{+0.9\dagger}_{-0.9}$	$120.9^{+17.1}_{-17.3}$	$147.1^{+16.0}_{-19.6}$	$1.8^{+0.1}_{-0.0}$ [115]	$0.5^{+0.0}_{-0.0}$ [115]	1.10 [116]
PSR J1311−3430	LM-PSR	62.5 ± 4.5 [117]	$2.4^{+0.5\dagger}_{-0.5}$	$108.6^{+16.6}_{-15.7}$	$156.8^{+27.4}_{-27.0}$	$2.1^{+0.1}_{-0.1}$ [117]	$0.0^{+0.0}_{-0.0}$ [117]	0.07 [118]
PSR J1417−4402	LM-PSR	-15.3 ± 0.9 [43]	$4.5^{+1.1}_{-0.8}$	$98.5^{+22.8}_{-19.0}$	$140.0^{+29.4}_{-23.6}$	$2.0^{+0.1}_{-0.1}$ [43]	$0.3^{+0.0}_{-0.0}$ [43]	5.37 [43]
PSR J1431−4715	LM-PSR	-91.0 ± 2.0 [108]	$1.6^{+0.3\dagger}_{-0.3}$	$122.8^{+18.4}_{-16.0}$	$114.3^{+22.1}_{-19.0}$	1.4*	>0.1 [119]	0.45 [119]
PSR J1622−0315	LM-PSR	-135.0 ± 6.0 [108]	$1.1^{+0.2\dagger}_{-0.2}$	$144.4^{+11.1}_{-10.3}$	$140.9^{+20.1}_{-26.1}$	>1.4 [108]	>0.1 [108]	0.16 [120]
PSR J1628−3205	LM-PSR	-4.0 ± 7.0 [108]	$1.2^{+0.2\dagger}_{-0.2}$	$114.1^{+28.4}_{-28.3}$	$150.8^{+40.9}_{-38.3}$	1.4*	>0.2 [121]	0.21 [108]
PSR J1653−0158	LM-PSR	-174.6 ± 5.1 [122]	$0.8^{+0.2\dagger}_{-0.2}$	$177.5^{+10.3}_{-9.4}$	$186.8^{+22.8}_{-40.0}$	$2.2^{+0.2}_{-0.1}$ [123]	$0.0^{+0.0}_{-0.0}$ [123]	0.05 [123]
PSR J1723−2837	LM-PSR	33.0 ± 2.0 [108]	$0.9^{+0.0}_{-0.0}$	$110.4^{+10.8}_{-10.6}$	$155.0^{+13.8}_{-33.0}$	$1.2^{+0.3}_{-0.2}$ [124]	$0.4^{+0.1}_{-0.1}$ [108]	0.62 [125]
PSR J1816+4510	LM-PSR	-99.0 ± 8.0 [126]	$4.4^{+0.9\dagger}_{-0.9}$	$165.3^{+30.6}_{-26.3}$	$170.3^{+24.6}_{-19.1}$	>1.8 [126]	>0.2 [126]	0.36 [127]
PSR J2039−5617	LM-PSR	6.0 ± 3.0 [108]	$1.8^{+0.4\dagger}_{-0.4}$	$113.5^{+27.8}_{-27.8}$	$164.5^{+40.5}_{-38.3}$	$1.3^{+0.3}_{-0.2}$ [128]	$0.2^{+0.0}_{-0.0}$ [128]	0.23 [128]
PSR J2129−0429	LM-PSR	-64.0 ± 2.0 [129]	$2.1^{+0.4}_{-0.3}$	$201.3^{+33.3}_{-24.2}$	$180.3^{+33.0}_{-35.5}$	$1.7^{+0.2}_{-0.2}$ [129]	$0.4^{+0.0}_{-0.0}$ [129]	0.64 [129]
PSR J2215+5135	LM-PSR	49.0 ± 8.0 [130]	$2.8^{+0.6\dagger}_{-0.6}$	$117.8^{+17.4}_{-17.4}$	$103.8^{+19.7}_{-20.2}$	$2.3^{+0.2}_{-0.1}$ [108]	$0.3^{+0.0}_{-0.0}$ [130]	0.17 [108]
PSR J2339−0533	LM-PSR	-49.0 ± 8.0 [131]	$1.1^{+0.2\dagger}_{-0.2}$	$64.1^{+13.5}_{-12.9}$	$97.5^{+18.1}_{-16.7}$	$1.6^{+0.3}_{-0.2}$ [132]	$0.3^{+0.1}_{-0.1}$ [108]	0.19 [132]
J05215658	BH-HMNI	-0.4 ± 0.1 [133]	$2.5^{+0.1}_{-0.1}$	$24.8^{+4.2}_{-2.6}$	$28.2^{+2.9}_{-2.8}$	$3.3^{+1.1}_{-0.4}$ [133]	$3.2^{+0.4}_{-0.5}$ [133]	83.20 [133]
J06163552	NS-LMNI	29.2 ± 0.7 [134]	$1.0^{+0.0}_{-0.0}$	$17.0^{+4.8}_{-2.6}$	$25.1^{+21.7}_{-10.0}$	$1.3^{+0.1}_{-0.1}$ [134]	$1.7^{+0.1}_{-0.1}$ [134]	0.87 [134]
J112306.9	NS-LMNI	-8.0 ± 2.0 [135]	$0.3^{+0.0}_{-0.0}$	$29.5^{+10.5}_{-10.3}$	$54.2^{+44.0}_{-24.7}$	$1.2^{+0.0}_{-0.0}$ [135]	$0.6^{+0.0}_{-0.0}$ [135]	0.27 [135]

Table 3 – *continued*

Name	Class	γ ($\mathrm{km\,s^{-1}}$)	d (kpc)	$v_{\rm pec,\,p}$ ($\mathrm{km\,s^{-1}}$)	$v_{\rm pec}^{z=0}$ ($\mathrm{km\,s^{-1}}$)	M_1 ($\mathrm{M_\odot}$)	M_2 ($\mathrm{M_\odot}$)	$P_{\rm orb}$ (d)
(1)	(2)	(3)	(4)	(5)	(6)	(7)	(8)	(9)
J125556.57	NS-LMNI	-3.4 ± 0.3 [136]	$0.5^{+0.0}_{-0.0}$	$36.1^{+7.1}_{-5.2}$	$45.1^{+4.0}_{-4.2}$	$1.4^{+0.7}_{-0.3}$ [136]	$1.2^{+0.1}_{-0.1}$ [136]	2.76 [136]
Gaia BH2	BH-LMNI	-4.2 ± 0.2 [137]	$1.2^{+0.0}_{-0.0}$	$25.2^{+9.7}_{-8.7}$	$34.1^{+5.0}_{-5.1}$	$8.9^{+0.3}_{-0.3}$ [137]	$1.1^{+0.2}_{-0.2}$ [137]	1276.70 [137]
J15274848	NS-LMNI	-26.1 ± 0.7 [138]	$0.1^{+0.0}_{-0.0}$	$13.8^{+7.1}_{-3.5}$	$18.9^{+3.1}_{-3.0}$	$1.0^{+0.1}_{-0.1}$ [138]	$0.6^{+0.1}_{-0.1}$ [138]	0.26 [139]
Gaia BH1	BH-LMNI	45.5 ± 0.8 [140]	$0.5^{+0.0}_{-0.0}$	$76.4^{+4.0}_{-3.1}$	$71.3^{+9.2}_{-10.8}$	$9.8^{+0.2}_{-0.2}$ [140]	$0.9^{+0.1}_{-0.1}$ [140]	185.59 [140]
AS 386	BH-HMNI	-31.8 ± 2.6 [141]	$5.9^{+0.5}_{-0.4}$	$10.8^{+8.0}_{-4.4}$	$20.6^{+2.2}_{-2.7}$	>7.0 [141]	$7.0^{+1.0}_{-1.0}$ [141]	131.27 [141]
J235456.76	NS-LMNI	41.0 ± 2.4 [142]	$0.1^{+0.0}_{-0.0}$	$47.9^{+9.4}_{-8.7}$	$52.5^{+7.6}_{-7.7}$	>1.3 [142]	$0.7^{+0.1}_{-0.1}$ [142]	0.48 [142]

References: [1] Jonker et al. (2005), [2] Steeghs & Jonker (2007), [3] Ashcraft, Hynes & Robinson (2012), [4] Cornelisse et al. (2013), [5] Díaz Trigo et al. (2009), [6] Shahbaz, Watson & Dhillon (2014), [7] Steeghs & Casares (2002), [8] Cherepashchuk, Khruzina & Bogomazov (2021), [9] LaSala & Thorstensen (1985), [10] Casares et al. (2006), [11] Reynolds et al. (1997), [12] Ponti et al. (2018), [13] Iaria et al. (2018), [14] Hinkle et al. (2019), [15] Hinkle et al. (2006), [16] Wang et al. (2017), [17] Casares et al. (2003), [18] Muñoz-Darias, Casares & Martínez-Pais (2005), [19] Jonker & van der Klis (2001), [20] Mata Sánchez et al. (2017), [21] Premachandra et al. (2016), [22] González-Galán et al. (2014), [23] den Hartog et al. (2004), [24] Grundstrom et al. (2007a), [25] Reig et al. (1996), [26] Crampton, Hutchings & Cowley (1985), [27] Sarty et al. (2009), [28] Reig et al. (1997), [29] Aragona et al. (2009), [30] Casares et al. (2005), [31] Gregory (2002), [32] Grundstrom et al. (2007b), [33] Delgado-Martí et al. (2001), [34] Barsukova et al. (2005), [35] Gontcharov (2006), [36] Hutchings (1984), [37] Priedhorsky & Terrell (1983), [38] Moritani et al. (2018), [39] Aragona, McSwain & De Becker (2010), [40] Gamen et al. (2015), [41] Stickland, Lloyd & Radziun-Woodham (1997), [42] Falanga et al. (2015), [43] Strader et al. (2015), [44] Waisberg & Romani (2015), [45] An et al. (2015), [46] van der Meer et al. (2007), [47] Nagase (1989), [48] Hutchings et al. (1987), [49] Ray & Chakrabarty (2002), [50] Kharchenko et al. (2007), [51] Stevens et al. (1997), [52] Kaper, van der Meer & Najarro (2006), [53] Waters et al. (1989), [54] Abubekerov, Antokhina & Cherepashchuk (2004), [55] Davison, Watson & Pye (1977), [56] Gies & Bolton (1986), [57] Islam & Paul (2016), [58] Nikolaeva et al. (2013), [59] Bikmaev et al. (2017), [60] Chojnowski et al. (2017), [61] Hambaryan et al. (2022), [62] González Hernández & Casares (2010), [63] Cantrell et al. (2010), [64] González Hernández, Rebolo & Casares (2014), [65] González Hernández et al. (2008b), [66] Khargharia et al. (2013), [67] Wu et al. (2015), [68] Wu et al. (2016), [69] González Hernández et al. (2017), [70] Mata Sánchez et al. (2021), [71] Casares et al. (2004), [72] Casares et al. (2009), [73] Orosz et al. (1998), [74] Orosz (2003), [75] Orosz et al. (2002), [76] Orosz et al. (2011), [77] González Hernández, Rebolo & Israelian (2008a), [78] Shahbaz (2003), [79] van der Hooft et al. (1998), [80] Heida et al. (2017), [81] Harlaftis et al. (1997), [82] Remillard et al. (1996), [83] Neustroev et al. (2014), [84] Shaw et al. (2016), [85] Zurita et al. (2008), [86] Torres et al. (2019), [87] Torres et al. (2020), [88] Russell et al. (2014), [89] Reid et al. (2014b), [90] Steeghs et al. (2013), [91] Casares & Charles (1994), [92] Khargharia, Froning & Robinson (2010), [93] Casares et al. (2019), [94] Gomez & Grindlay (2021), [95] MacDonald et al. (2014), [96] Orosz et al. (2001), [97] Picchi et al. (2020), [98] Crampton & Hutchings (1981), [99] Gies et al. (2008), [100] Miller-Jones et al. (2021), [101] LaSala et al. (1998), [102] Casares et al. (2012), [103] Williams et al. (2010), [104] Antoniadis et al. (2013), [105] Callanan, Garnavich & Koester (1998), [106] Nicastro et al. (1995), [107] Thorstensen & Armstrong (2005), [108] Strader et al. (2019), [109] Archibald et al. (2013), [110] Bassa et al. (2016), [111] Kaplan et al. (2016), [112] Deneva et al. (2016), [113] de Martino et al. (2014), [114] Miller-Jones et al. (2018), [115] Swihart et al. (2019), [116] Linares et al. (2018), [117] Romani (2012), [118] Romani et al. (2012), [119] Bates et al. (2015), [120] Sanpa-Arsa (2016), [121] Ray et al. (2012), [122] Romani, Filippenko & Cenko (2014), [123] Nieder et al. (2020), [124] van Staden & Antoniadis (2016), [125] Crawford et al. (2013), [126] Kaplan et al. (2013), [127] Stovall et al. (2014), [128] Clark et al. (2021), [129] Bellm et al. (2016), [130] Linares (2018), [131] Romani & Shaw (2011), [132] Pletsch & Clark (2015), [133] Thompson et al. (2019), [134] Yuan et al. (2022), [135] Yi et al. (2022), [136] Mazeh et al. (2022), [137] El-Badry et al. (2023a), [138] Lin et al. (2023), [139] Jayasinghe et al. (2019), [140] El-Badry et al. (2023b), [141] Khokhlov et al. (2018), [142] Zheng et al. (2022)

† Literature distance ($d_{\rm lit}$; Table S1) used because the parallax is not well constrained or not available (Section 2.7); for PSRs, these are distances inferred from the Yao, Manchester & Wang (2017) dispersion measures.

* Values that have no literature constraints.

0.9 and 1.2, respectively (for a satisfactory fit to a single-star model, `ruwe` is expected to be close to 1).[5]

The distance to 2A 1822−371 was estimated to be between 2 and 3 kpc based on the emitting region area at peak brightness of the light curve, while assuming a blackbody for the inner emitting region gives an upper limit of ≈ 5 kpc (Mason & Cordova 1982), which is marginally consistent with our estimate at the 68 per cent level.

Khokhlov et al. (2018, K18) estimated a distance of 2.4 ± 0.3 kpc for AS 386, which is less than half of its d_{ϖ} ($5.9^{+0.5}_{-0.4}$ kpc). The K18 estimate is based on a fitted extinction law and an estimated reddening of ≈0.9. However, with the updated 3D 'Bayestar19' dust map (Green et al. 2019), we get a similar reddening at a larger distance of at least 4.7 kpc (calculated using the DUSTMAP package; see Green 2018). We thus adopt our estimate of distance even though the astrometric solution is mildly argued against by its `ruwe` value.

3.2 Distribution of peculiar velocities

With the calculated $v_{\rm pec}^{z=0}$ samples, the first analysis we can do is to get an overview of their distribution among different subclasses. We therefore divide our compilation into four subgroups, including (1) binaries with BHs, (2) binaries with NSs, (3) binaries with LM companions, and (4) binaries with HM companions. With the calculated $v_{\rm pec}^{z=0}$ distributions of individual binaries, we model the overall $v_{\rm pec}^{z=0}$ distribution for these subgroups following a Bayesian approach. Given a binary class, we first construct 1000 bootstrapped data sets for each subgroup by randomly sampling (with replacement) from the individual $v_{\rm pec}^{z=0}$ distributions. The Bayesian model is constructed as follows: for the likelihood, we use a Maxwellian

[5] *Gaia* pipeline flags, including `ruwe` and `astrometric excess noise`, provide an estimate of the quality of the astrometric fit, but these are degenerate with non-single star solutions (cf., Belokurov et al. 2020; Gandhi et al. 2022), so we purposely do not preselect on these flags.

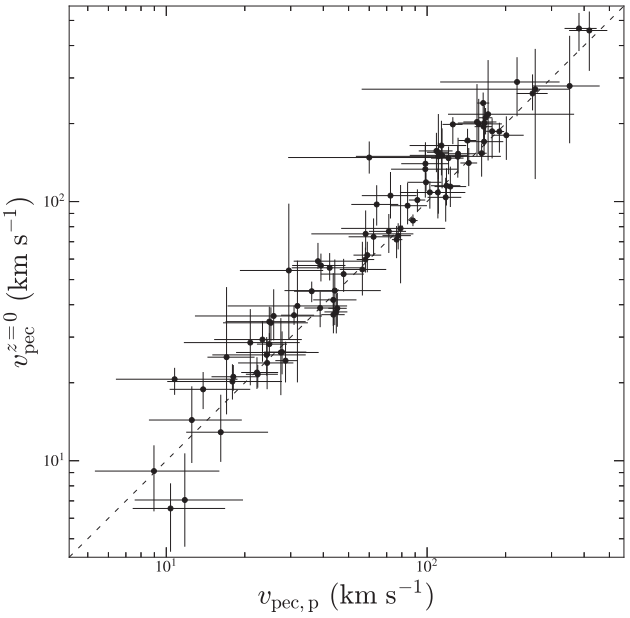

Figure 1. Median values of present-day peculiar velocity ($v_{\rm pec,\,p}$) versus those of potential peculiar velocity at birth ($v_{\rm pec}^{z=0}$) for binaries that have measured systemic radial velocity. The error bars correspond to 16th and 84th percentiles of the distributions. The dashed line indicates $v_{\rm pec,\,p} = v_{\rm pec}^{z=0}$. Overall, $v_{\rm pec}^{z=0}$ values agree with $v_{\rm pec,\,p}$ at 68 per cent level.

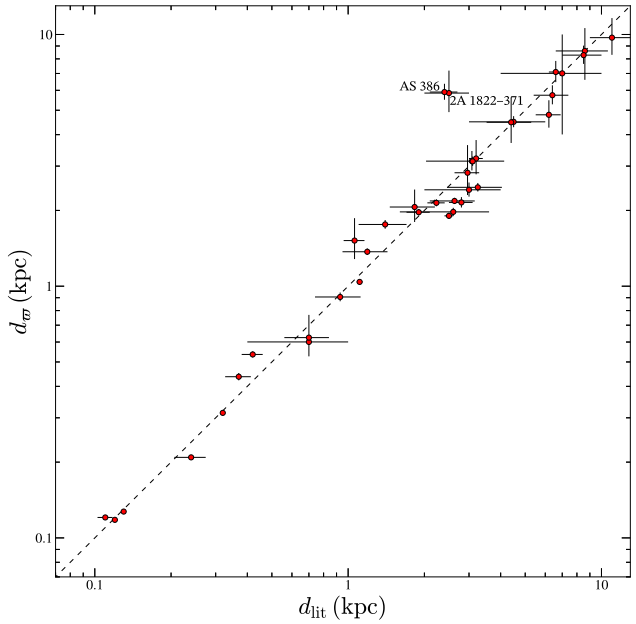

Figure 2. A comparison between literature distances ($d_{\rm lit}$) and parallax-inferred distances (d_ϖ), showing that they agree for most binaries. The error bars on d_ϖ correspond to 68 per cent confidence intervals. The two obvious outliers are labelled with their names.

distribution:

$$f(v|\sigma_v) = \sqrt{\frac{2}{\pi}}\frac{v^2}{\sigma_v^3}\exp\left(-\frac{v^2}{2\sigma_v^2}\right), \tag{6}$$

where σ_v is the scale parameter, or a two-component Maxwellian distribution:

$$f(v|\sigma_{v,1}, \sigma_{v,2}, w) = wf(v|\sigma_{v,1}) + (1-w)f(v|\sigma_{v,2}), \tag{7}$$

where w is a weighting factor that determines contribution of the single Maxwellians that are characterized by $\sigma_{v,1}$ and $\sigma_{v,2}$, respectively. We use uninformative (flat) priors for all parameters: for a two-component Maxwellian likelihood, a flat prior between 0 and 100 kms^{-1} ($U(0, 100)$) is used for low-velocity component, while $U(0, 500)$ is used to represent the high-velocity component; for the single-component Maxwellian, we choose $U(0, 500)$ for the only scale parameter σ_v.

The established posterior given the bootstrapped data set is then sampled with a Markov Chain Monte Carlo (MCMC) algorithm using the PYMC (version 5.0.2) package (Salvatier, Wieckiâ & Fonnesbeck 2016), which applies the No-U-Turn Sampler (Hoffman & Gelman 2011). We set up four chains and run each chain for 3000 iterations including 1000 for tuning; convergence is checked using the Gelman-Rubin diagonistic ($\hat{R}$; Gelman & Rubin 1992, converged chains should have $\hat{R} \approx 1$). We check $\hat{R}$ for each bootstrapped data set and consider simulations that have relative deviation of $\hat{R}$ from unity greater than 0.01 (i.e. $|\hat{R} - 1|/\hat{R} \geq 0.01$) as diverging chains.

For model comparison, we use the ARVIZ package (Kumar et al. 2019) to compute the leave-one-out (LOO) cross-validation (Vehtari, Gelman & Gabry 2017) for the bootstrapped data sets; the computation assigns a LOO weight ($w_{\rm loo}$) to the single- and two-component Maxwellian fit to represent relative support for each model given the observed data, with $w_{\rm loo}$ closer to 1 being more favoured. As a complementary diagnostic, we also compute the fraction of diverging chains for each parameter, which is denoted as $f_{\rm diverge}$. Chains not converging could be a result of insufficient iterations, or simply because the assumed likelihood is not appropriate for the underlying population. In this regard, $f_{\rm diverge}$ can be used as a diagnostic for the suitability of the specified model. Table 4 summarises median and credible intervals of the posterior for the hyper-parameters, and in Fig. 3, we show the distribution of median $v_{\rm pec}^{z=0}$ overplotted with the models.

Our results show that a two-component Maxwellian distribution gives a sensible fit to all binaries as a whole, with $\hat{R}$ consistent within 10^{-4} of 1 for all simulations (i.e. $f_{\rm diverge} = 0$). All bootstrapped data sets strongly favour a two-component model ($w_{\rm loo} = 1$) over a single Maxwellian ($w_{\rm loo} = 0$). The posterior gives a low- and a high-$v_{\rm pec}^{z=0}$ component that are characterized by $\sigma_{v,1} = 21 \pm 3$ kms^{-1} and $\sigma_{v,2} = 107^{+10}_{-9}$ kms^{-1}, respectively (uncertainties correspond to 68 per cent credible level, and the same for other quoted parameters in this section). This two-component Maxwellian also applies to the NS subgroup, with a low- and high-velocity component at $\sigma_{v,1} = 21^{+4}_{-3}$ kms^{-1} and $\sigma_{v,2} = 113^{+12}_{-11}$ kms^{-1}, and $w_{\rm loo}$ also favours two-components ($w_{\rm loo} = 1$) over a single Maxwellian ($w_{\rm loo} = 0$). The two-component model also gives a higher $w_{\rm loo}$ weight when applied to the BH subgroup; however, it leads to divergence in over 44 per cent of the simulations; we thus conclude that the existence of a second component in BH subgroup is insignificant, given the current sample.

Applying a two-component Maxwellian model to fit the LM and HM subgroups also leads to non-negligible divergence in over 26 per cent and 34 per cent of the simulations, respectively; whereas a single Maxwellian fits the data without divergence, giving very distinct σ_v at 101^{+8}_{-7} kms^{-1} and 27 ± 2 kms^{-1} for LM and HM binaries, respectively. By visual inspection, the HM subgroup seems to be restricted below 100 kms^{-1}, while the LM group shows a broader distribution up to a velocity of ≈ 400 kms^{-1} (Fig. 3). Despite

Table 4. Parameters of Maxwellian distribution from MCMC sampling.

Class	Model	$\sigma_{v,1}$ (kms^{-1})	$\sigma_{v,2}$ (kms^{-1})	w	$f^{a}_{\rm diverge}$ (per cent)
BH	Single Maxwellian	$64.2^{+8.5}_{-7.5}$	...	...	(0.0)
	Two Maxwellians	$26.1^{+28.0}_{-7.0}$	$87.4^{+29.1}_{-25.6}$	$0.5^{+0.2}_{-0.2}$	(46, 45, 36)
NS	Single Maxwellian	$85.5^{+6.5}_{-6.1}$	...	...	(0)
	Two Maxwellians	$20.9^{+3.8}_{-3.3}$	$112.7^{+12.5}_{-10.9}$	$0.4^{+0.1}_{-0.1}$	(0, 0, 0)
LM	Single Maxwellian	$100.8^{+7.9}_{-7.3}$	...	...	(0)
	Two Maxwellians	$73.5^{+9.5}_{-24.7}$	$177.3^{+80.1}_{-57.5}$	$0.8^{+0.1}_{-0.4}$	(30, 29, 28)
HM	Single Maxwellian	$27.1^{+2.3}_{-2.1}$	...	...	(0)
	Two Maxwellians	$15.9^{+6.4}_{-2.4}$	$40.7^{+9.8}_{-12.0}$	$0.6^{+0.1}_{-0.2}$	(49, 49, 47)
All	Single Maxwellian	$80.5^{+5.3}_{-5.0}$	...	...	(0)
	Two Maxwellian	$21.3^{+3.3}_{-2.8}$	$106.7^{+10.4}_{-9.2}$	$0.4^{+0.1}_{-0.1}$	(0, 0, 0)

[a] $f_{\rm diverge}$ values in parentheses correspond to the parameters in columns 3–5.

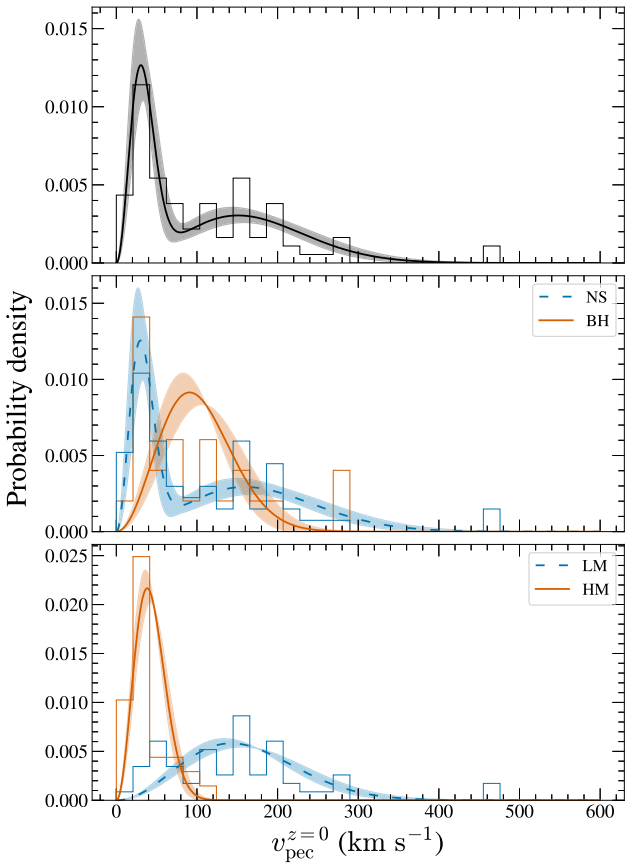

Figure 3. Distribution of $v_{\rm pec}^{z=0}$ values of all binaries in Table 3 (top), binaries that host a BH or NS (middle), and binaries that host an HM or LM non-degenerate companion (bottom). The solid lines in each panel represent the single- or two-component Maxwellian model characterised by the median parameters, while the shaded band represents the 68 per cent credible region propagated from the parameter posteriors.

the divergence fractions, the LOO diagnostic still favours a two-component ($w_{\rm loo} = 1$) over a single Maxwellian ($w_{\rm loo} \approx 10^{-15}$) for both LM and HM subgroups; this could be due to biases in $w_{\rm loo}$ estimate for smaller sample sizes (Vehtari et al. 2017), so more robust conclusion can be made with more future identification of systems in each class.

3.3 Comparing distributions of peculiar velocities

There is some difference between the LM and HM subgroups and possibly also between the BH and NS subgroups, as suggested by our MCMC fits (Section 3.2). These differences could relate to the possibility that different NK mechanisms apply to binaries with different compact objects; more importantly, it has been long suggested that observed recoil velocity is dependent on masses (component mass or total mass) following conservation of NK momentum, which might also lead to distinct distributions.

To investigate possible indication, we start by testing potential differences in distributions of $v_{\rm pec}^{z=0}$ between subgroups. Since $v_{\rm pec}^{z=0}$ has a rather strong dependence on distance ($v_{\rm pec}^{z=0} \propto d$), we use the 85 binaries that have relatively well-defined distances (either from literature or inferred from *Gaia* parallaxes). For each binary, we randomly draw (with replacement) 10 000 velocities from the $v_{\rm pec}^{z=0}$ sample of Section 2.9 and perform two-tailed Kolmogorov–Smirnov (K-S) tests comparing BH versus NS and LM versus HM binaries at a pre-defined significance level (α) of 0.01, using the `ks_2sample` function in the SCIPY package[6] (Virtanen et al. 2020).

As a measure of the significance of the difference, we calculate the fraction of simulations rejecting the null hypothesis (denoted by $f_{\rm rej}$) that the two samples are drawn from the same underlying distribution. In Table 5, we summarise medians and uncertainties for the resulting test statistics and p-values, and in Fig. 4, we present cumulative distributions comparing different subgroups.

Comparing $v_{\rm pec}^{z=0}$ distributions between subgroups suggests no difference between NS and BH binaries at a significance level of 0.01 ($f_{\rm rej} = 0$); we further compare BH and NS binaries for the LM and HM subgroups and still find no difference in their $v_{\rm pec}^{z=0}$ distributions. However, we find a marked difference between the LM and HM subgroups ($f_{\rm rej} = 100$ per cent), suggesting that HM binaries are from a population with lower $v_{\rm pec}^{z=0}$ compared to the LM group. This is in line with our Maxwellian fits to the LM and HM subgroups, where the majority of the HM binaries have median $v_{\rm pec}^{z=0} \lesssim 100\,{\rm kms}^{-1}$ (Fig. 3), with the highest being Cen X-3 ($v_{\rm pec}^{z=0} = 108 \pm 10\,{\rm kms}^{-1}$), while the LM binaries have $v_{\rm pec}^{z=0}$ up to ~400 kms. This difference is mostly

[6] https://scipy.org/

Table 5. Two-sample K-S test results comparing $v_{\rm pec}^{z=0}$ between different classes.

Subgroups	Sample sizes	Test statistic	p-value	$f_{\rm rej}^{a}$ (per cent)
NS versus BH	63, 22	0.20 ± 0.04	0.48 ± 0.22	0
LM versus HM	52, 33	0.67 ± 0.02	$\leq 2.22 \times 10^{-8}$	100
NS-LM versus BH-LM	37, 15	0.37 ± 0.06	0.10 ± 0.09	4.6
NS-HM versus BH-HM	26, 7	0.27 ± 0.06	0.73 ± 0.20	0
NS-LM versus NS-HM	37, 26	0.74 ± 0.03	$\leq 8.78 \times 10^{-8}$	100
BH-LM versus BH-HM	15, 7	0.66 ± 0.08	≤ 0.04	37.4

[a]: Percentage of simulations that reject the null hypothesis at the given significance level (1 per cent).

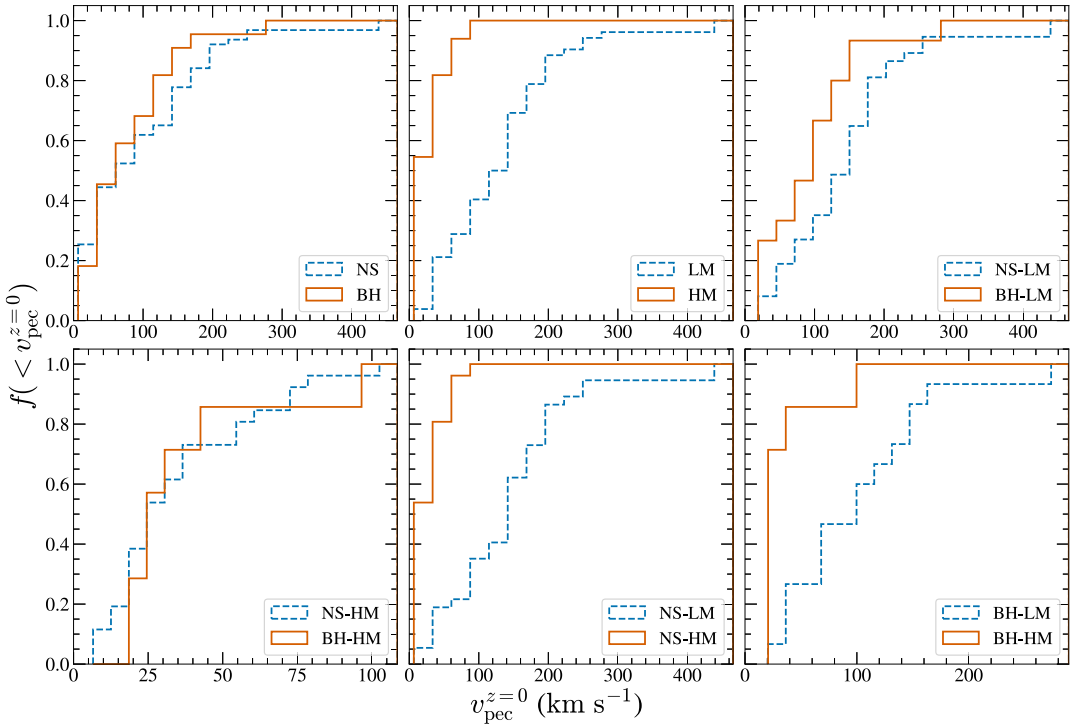

Figure 4. Cumulative distributions of median $v_{\rm pec}^{z=0}$ for different binary subgroups.

contributed by the NS binaries in our sample as the difference persists for NS-LM versus NS-HM ($f_{\rm rej} = 100$ per cent) but is much less significant for BH-LM versus BH-HM ($f_{\rm rej} = 37$ per cent; Table 5).

3.4 Mass and peculiar velocity

The distinct distributions of LM versus HM binaries suggest an anticorrelation of $v_{\rm pec}^{z=0}$ on M_2, while no strong dependence of $v_{\rm pec}^{z=0}$ on M_1, as the K-S test of NS versus BH subgroups suggests no significant difference. With greater inertia, more massive binaries are harder to be accelerated, $v_{\rm pec}^{z=0}$ (recoil obtained from NK) is expected to be negatively correlated with mass. Indeed, efforts have been made to find possible anticorrelation between peculiar velocity and binary component masses (e.g. Fryer & Kalogera 2001; Fryer et al. 2012; Mirabel 2017; Atri et al. 2019; Gandhi et al. 2019); however, past studies mostly focused only BH XRBs, and the peculiar velocities are only compared with BH masses (M_1). While M_1 is close to $M_{\rm tot}$ in BH-LMXBs, M_2 should be also be taken into account, especially for binaries with massive companions (e.g. Cyg X-1). It is therefore more natural to investigate this potential correlation with $M_{\rm tot}$.

We therefore pick binaries that have either constrained values or sensible estimates on M_1 and M_2 for our analysis. More specifically, a binary is included if it has a constrained value on M_1 and M_2, or if either M_1 or M_2 has a lower limit while the other mass is constrained. Some binaries have no measurement of M_1 but the compact object has been confirmed to be an NS (e.g. by detection of pulsations); if such a binary has a constrained or just a lower limit on M_2, we also include it in the analysis and assume a canonical NS mass of $1.4\,{\rm M}_{\odot}$ for M_1 with a 20 per cent uncertainty. We then follow two methods

to test for possible correlation: (1) fitting a log-linear model to, and (2) calculating the Pearson's ($\rho_{\rm p}$) and Spearman's ($\rho_{\rm s}$) correlation coefficient for bootstrapped velocities and Monte Carlo samples of $M_{\rm tot}$.

We bootstrapped 1000 velocities from the calculated $v_{\rm pec}^{z=0}$ distribution (Section 2.9) for each of these binaries. To account for uncertainties in $M_{\rm tot}$, we sample from a log-normal distribution that centres at the logarithm of the literature value with a standard deviation set to the maximum between upper and lower error; we also include binaries that only have lower limits on $M_{\rm tot}$; for these lower limits, we sample from a log-uniform distribution spanning from the lower limit ($M_{\rm tot,\,lolim}$) to $2M_{\rm tot,\,lolim}$.

We then follow a Bayesian approach to fit log-linear models to the 1000 bootstrapped data set. We assume a likelihood ($\mathcal{L}$) that joins binary-specific Gaussian likelihoods $N(\mu_i, \sigma_i)$, i.e.:

$$\begin{aligned}\mathcal{L} &= \prod_i N(\mu_i, \sigma_i)\\ \mu_i &= \theta_{0,M_{\rm tot}} + \theta_{1,M_{\rm tot}}\left(\log M_{{\rm tot},i} - \overline{\log M_{\rm tot}}\right)\\ \sigma_i^2 &= \sigma_{v,i}^2 + \left(f_{\rm err}\log v_{{\rm pec},i}^{z=0}\right)^2,\end{aligned} \tag{8}$$

Here, $\theta_{0,M}$ and $\theta_{1,M}$ are the fit parameters; $\log M_{\rm tot}$ in the model is offset by the mean ($\overline{\log M_{\rm tot}}$) over each bootstrapped data set to remove covariance between the two coefficients; $\sigma_{v,i}$ characterizes the intrinsic uncertainty in our calculated distribution, which we set to the maximum between offsets of 16th and 84th percentiles from the median (i.e. the maximum between upper and lower errors reported in Table 3); we further inflate the uncertainty by assuming that it is underestimated by some fractional value $f_{\rm err}$. We use flat priors for all hyperparameters: $\theta_{0,M_{\rm tot}} \sim U(-5, 5)$, $\theta_{1,M_{\rm tot}} \sim U(-5, 5)$, and $f_{\rm err} \sim U(0, 1)$. The sampling is then performed with PYMC using the same configuration for the sampler as in Section 3.2. All chains have good convergence with $|\hat{R} - 1|/\hat{R} < 0.001$, and samples from all MCMC runs are concatenated and presented in Fig. 5. The fit results (Table 6) strongly suggest a negative slope ($\theta_{1,M_{\rm tot}}$), with a 99.7 per cent credible interval ranging from -0.84 to -0.16; the fit also suggests a moderate error fraction $f_{\rm err} = 0.20$, indicating some additional uncertainty to the measured velocities. In Fig. 6, we show the scatters of $v_{\rm pec}^{z=0}$ vs. $M_{\rm tot}$ and the best-fit log-linear model.

With the simulated data, we use SCIPY to calculate $\rho_{\rm p}$ and $\rho_{\rm s}$ and the associated p-values. As a point of comparison, we also calculate the coefficients with velocities sampled from distributions that are 'smeared' by $f_{\rm err}$ per cent additional error (in Table 6). When no additional error is included, all simulations yield a negative coefficient, hinting at a significant anticorrelation (Table 7); a more sensible measure of robustness is the p-value; here, we compare the p-values to an *a priori* significance level of 1 per cent and calculate $f_{\rm rej}$ (fraction of simulations that reject the null hypothesis; Section 3.3). When no additional error is incorporated, all simulations favour an anticorrelation according to the results using $\rho_{\rm p}$ and $\rho_{\rm s}$, respectively. $f_{\rm rej}$ drops to a lower percentage of 85 per cent (or 84 per cent for $\rho_{\rm s}$) when a fraction of $f_{\rm err}$ additional errors is added to $v_{\rm pec}^{z=0}$ that still suggests a significant negative correlation.

3.5 Orbital period and peculiar velocity

The binaries in our compilation all survived their NKs; their observed orbital periods ($P_{\rm orb}$) can give insights on how tightly bound they were and thus on distribution of NK magnitudes. We thus also include known $P_{\rm orb}$ in the compilation (Table 3).

It is also interesting to check if $P_{\rm orb}$ and $v_{\rm pec}^{z=0}$ show any evidence of dependences, so we follow a Bayesian approach similar to that in Section 3.4 to fit the data. The intercept and slope are denoted as $\theta_{0,P_{\rm orb}}$ and $\theta_{1,P_{\rm orb}}$. This model is applied to simulated data generated by a similar bootstrapping process as in Section 3.4, i.e. for each binary that has a well measured $P_{\rm orb}$; we sample 1000 velocities from the calculated distribution; the only difference here is that we do not simulate $P_{\rm orb}$ but use the literature $P_{\rm orb}$ values for all simulated velocities as the compiled $P_{\rm orb}$'s are all tightly constrained (median fractional error of 5×10^{-6}). The fit result suggests a negative slope of -0.19 with a 99.7 per cent credible interval between -0.29 and -0.09. We plot the distribution of model parameters in Fig. 5 and plot the scatters of $v_{\rm pec}^{z=0}$ and $P_{\rm orb}$ in Fig. 7.

Following the same approach, we also calculate the $\rho_{\rm s}$ and $\rho_{\rm p}$ for $v_{\rm pec}^{z=0}$ versus $P_{\rm orb}$. The correlation is significant as all simulations yield p-values below 1 per cent, and even with additional uncertainty in $v_{\rm pec}^{z=0}$, the $f_{\rm rej}$ is still at a robust level (Table 7). We can therefore conclude that the anticorrelation between $v_{\rm pec}^{z=0}$ and $P_{\rm orb}$ is statistically significant.

4 DISCUSSION

Our statistical analyses together suggest a significant anti-correlation between $v_{\rm pec}^{z=0}$ and $M_{\rm tot}$, and between $v_{\rm pec}^{z=0}$ and $P_{\rm orb}$. In this section, we present some physical interpretation of these results and discuss possible observational and physical biases that could have contributed to our results.

4.1 Peculiar velocity versus binary total mass

NKs imparted on compact objects at SNe can be broadly attributed to two effects: recoil due to a sudden ejection of mass (also known as the 'Blaauw kick', Blaauw 1961) and/or any additional impulses of momentum on the compact object. The difference between the two is that the former conserves system (ejecta-binary) linear momentum, so binaries in which the companion star of the compact object is more massive would acquire a smaller $v_{\rm pec}^{z=0}$ if the ejecta momenta are comparable among different binaries. This can, however, be complicated by the fact that the orbital speeds of the SN progenitor can, in some cases, be faster in shorter-period binaries, which may be associated with lower mass companion stars. An impulse of an additional momentum beyond ejecta-induced recoil, on the other hand, is equivalent to having an external force on the compact object, so this conservation is no longer met. With an additional kick, even a massive binary can end up with high $v_{\rm pec}^{z=0}$ if the kick velocity is at a supportive magnitude and direction that keep the binary bound.

The kinematic formulation of $v_{\rm pec}^{z=0}$ was derived by Kalogera (1996; K96 hereafter) that incorporates the effect of both mass ejecta and additional kick velocity. According to K96, a bound binary that survived the SN gets a $v_{\rm pec}^{z=0}$ constrained between an upper and lower limit given by[7]:

$$\begin{aligned}v_{\rm pec,min}^{z=0}/V_r &= \frac{M_1+\Delta M}{M_{\rm tot}+\Delta M} - \frac{\sqrt{2}M_1}{M_{\rm tot}^{1/2}\,(M_{\rm tot}+\Delta M)^{1/2}}\\ v_{\rm pec,max}^{z=0}/V_r &= \frac{M_1+\Delta M}{M_{\rm tot}+\Delta M} + \frac{\sqrt{2}M_1}{M_{\rm tot}^{1/2}\,(M_{\rm tot}+\Delta M)^{1/2}},\end{aligned} \tag{9}$$

[7]Note that the equations are slightly different from the K96 version because we re-write it with the notations in this paper (Section D).

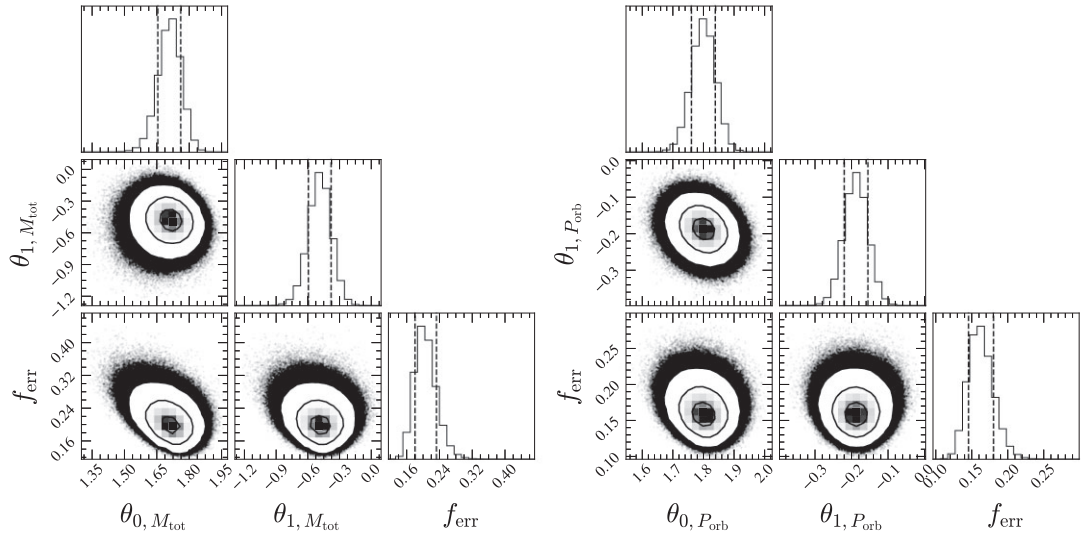

Figure 5. Corner plot made using the CORNER package (Foreman-Mackey et al. 2016) showing posterior distributions of fit parameters of $v_{\rm pec}^{z=0}$ versus $M_{\rm tot}$ (left) and $v_{\rm pec}^{z=0}$ versus $P_{\rm orb}$ (right). The contours in the projected distributions correspond to 1σ, 2σ, and 3σ levels. The vertical dashed lines in the marginal panels indicate 68 per cent credible intervals.

Table 6. Log-linear fit results, with 68 per cent confidence uncertainties.

$v_{\rm pec}^{z=0}$ versus	θ_0	θ_1	$f_{\rm err}$
$M_{\rm tot}$	1.71 ± 0.05	-0.48 ± 0.11	0.20 ± 0.03
$P_{\rm orb}$	1.80 ± 0.04	-0.19 ± 0.03	0.16 ± 0.02

where ΔM is the ejecta mass and V_r is the relative orbital velocity at SN. If one assumes a circular orbit,

$$V_r = 212.9 \left(\frac{M_{\rm tot} + \Delta M}{\rm M_\odot}\right)^{1/3} \left(\frac{P_{\rm orb,SN}}{\rm day}\right)^{-1/3} \ {\rm kms}^{-1}, \tag{10}$$

where $P_{\rm orb,\,SN}$ is the orbital period at the instant of SN. Physically, the upper limit is reached when the NK is in the opposite direction to the orbital velocity of the BH/NS progenitor at the instant of SN while keeping the binary bound; the lower limit, on the other hand, corresponds to the minimum possible NK on the compact object to keep the binary from being disrupted by mass ejection. Equations (9) and (10) immediately point to an anticorrelation with $M_{\rm tot}$; this simply indicates that more massive systems are harder to be accelerated by NKs.

One can also get the difference between the maximum and minimum $v_{\rm pec}^{z=0}$:

$$\begin{aligned} v_{\rm pec,max}^{z=0} - v_{\rm pec,min}^{z=0} &= \frac{2\sqrt{2}M_1}{M_{\rm tot}^{1/2}\,(M_{\rm tot}+\Delta M)^{1/2}} V_r \\ &\propto M_1 M_{\rm tot}^{-1/2}\,(M_{\rm tot}+\Delta M)^{-1/6}\,P_{\rm orb,SN}^{-1/3}. \end{aligned} \tag{11}$$

This difference is related to the width of $v_{\rm pec}^{z=0}$ distributions.

A simple comparison can then be performed between different binary subgroups hosting NSs, given that M_1 for these binaries are very similar. From equation (11), it immediately follows that NS-LMXBs exhibit a broader distribution compared to HMXBs because they have (1) more compact orbits at SN, (2) smaller progenitor (helium core) mass at SN thus less mass was ejected (smaller ΔM), and (3) apparently smaller $M_{\rm tot}$ values. The progenitors of LMXBs are thought to begin with a wide orbit that then dramatically shrinks through a common envelope (CE) process (Paczynski 1976). The shrunken orbits greatly increase the survivability against the coming SN and lead to higher $v_{\rm pec}^{z=0}$s. While some HMXBs could have a comparable pre-SN orbit (e.g. Cen X-3; see e.g. van den Heuvel & Heise 1972), the $M_{\rm tot}^{-1/2}\,(M_{\rm tot}+\Delta M)^{-1/6}$ factor contributes significantly considering a factor of few or even an order of magnitude difference in $M_{\rm tot}$.

Our compiled NS-LMXBs are within the 'allowed' range defined by the K96 limits (Fig. 8); however, we noted that all of them are above $\approx 50\,{\rm kms}^{-1}$, so the lower-left of Fig. 6 is clearly underpopulated. It was pointed out by Kalogera (1998) that some LMXBs could have originated from progenitors in wide orbits that then shrink if the kick velocity is at a favourable magnitude and direction; this 'direct-SN' scenario circumvents the need of a CE stage, and thus SN would occur at wide orbits, leading to low-$v_{\rm pec}^{z=0}$ (typically between $20-50\,{\rm kms}^{-1}$) binaries. Their absence could be a result of observational biases (see Section 4.4).

It is also worth noting that NIs that host NSs have systematically lower $v_{\rm pec}^{z=0}$ than NS-LMXBs, but the significance of this difference can only be addressed with a greater sample and more confident identifications of NS-NIs. Indeed, the nature of the compact object is yet ambiguous in some systems, as their M_1 can also overlap with the range for massive white dwarfs. Nevertheless, it is also possible that NS-NIs might have also been formed through the 'direct-SN' scenario similar to that for LMXBs, but the orbits were not perturbed sufficiently by the kick and shrunk enough for mass transfer to start. With the observed upper limit $\approx 60\,{\rm kms}^{-1}$ for $v_{\rm pec}^{z=0}$ and a $\Delta M = 1\,{\rm M}_\odot$, the progenitor has a $P_{\rm orb,SN} \approx 560$ d following equation (9). Efficiency of such scenario is beyond the scope of this paper and can be addressed by future population synthesis studies.

One can also compare the range of $v_{\rm pec}^{z=0}$ for subclasses of HMXBs. After the first mass-exchange stage (i.e. from the compact object progenitor to the companion), HMXBs with supergiant donors (SgXRBs) are thought to be in closer orbits (period could be as

Table 7. Pearson and Spearman's coefficients and the corresponding p-values. Uncertainties correspond to the 68 per cent confidence level.

$v_{\rm pec}^{z=0}$ versus	$\rho_{\rm p}$	p-value ($\rho_{\rm p}$)	$f_{\rm rej}$ (per cent)	$\rho_{\rm s}$	p-value ($\rho_{\rm s}$)	$f_{\rm rej}$ (per cent)
			With no additional error in $v_{\rm pec}^{z=0}$			
$M_{\rm tot}$	-0.52 ± 0.03	$4.69^{+15.05}_{-3.61} \times 10^{-6}$	100	-0.55 ± 0.03	$1.18^{+4.91}_{-0.96} \times 10^{-6}$	100
$P_{\rm orb}$	-0.53 ± 0.02	$6.68^{+15.31}_{-4.69} \times 10^{-7}$	100	-0.57 ± 0.02	$5.15^{+17.48}_{-4.11} \times 10^{-8}$	100
			With $f_{\rm err}$ per cent additional error in $v_{\rm pec}^{z=0}$			
$M_{\rm tot}$	-0.39 ± 0.08	$9.96^{+80.36}_{-9.20} \times 10^{-4}$	85	-0.39 ± 0.08	$9.09^{+90.90}_{-8.49} \times 10^{-4}$	84
$P_{\rm orb}$	-0.46 ± 0.06	$2.96^{+32.04}_{-2.80} \times 10^{-4}$	99	-0.50 ± 0.07	$5.81^{+108.85}_{-5.63} \times 10^{-6}$	99

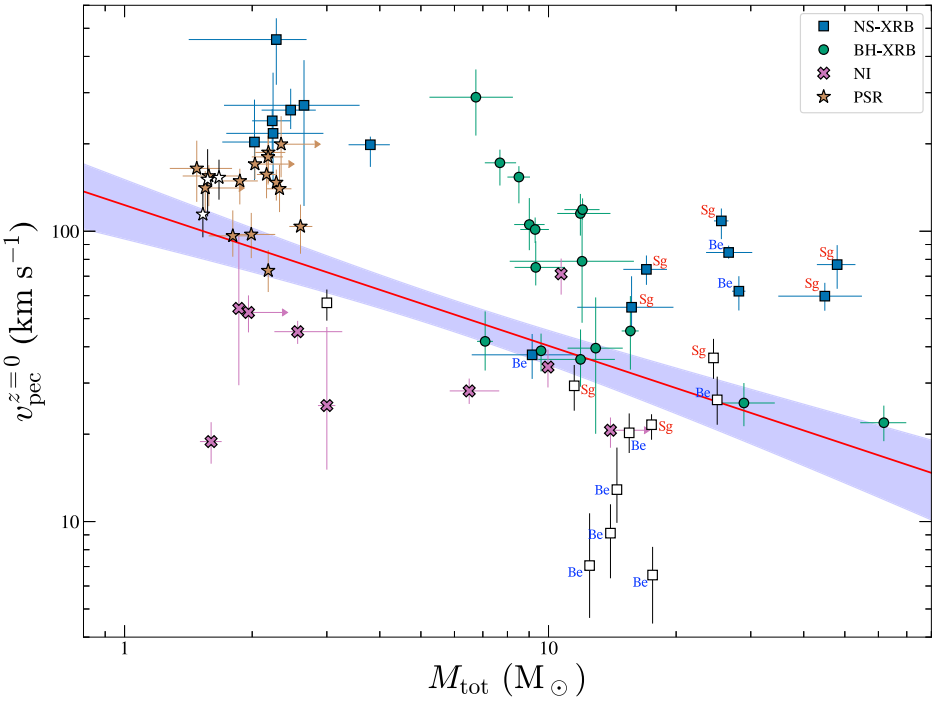

Figure 6. $v_{\rm pec}^{z=0}$ versus $M_{\rm tot}$ for binaries with constrained or lower limits on $M_{\rm tot}$ (filled markers) and those that have only approximate masses (empty markers with no error bars on $M_{\rm tot}$). The error bars of $v_{\rm pec}^{z=0}$ correspond to 16th and 84th percentiles. The red solid line indicates the best-fitting model (Section 3.4), with the blue shading indicating the 68 per cent confidence region. The NS-HMXBs are further distinguished between those that have a supergiant companion ('Sg') and a Be companion ('Be').

short as a few days; see e.g. De Loore et al. 1974), while those with Be stars (BeXRBs) could be much wider (periods of up to hundreds of days; e.g. Habets 1985). Although SgXRBs have slightly greater $M_{\rm tot}$ than BeXRBs, they are not drastically different. Therefore, $P_{\rm orb,\,SN}$ plays a more crucial role. As a result, $v_{\rm pec}^{z=0}$ for BeXRBs should be systematically downscaled by V_r compared to SgXRBs. This distinction has been suggested by past studies (van den Heuvel et al. 2000; Fortin et al. 2022) and will be tested with future statistical analyses (Nuchvanichakul et al., in preparation).

In all, the decreasing trend with increasing $M_{\rm tot}$ could be roughly attributed to increasing inertia of binaries, regardless of additional kick velocity; this trend can also be guided by the K96 limits assuming some orbital parameters at SN for subgroups of binaries. To visualise this, in Fig. 8, we plot K96 limits for different types of binaries assuming some typical parameters at SN (Table 8), where we further distinguish between SgXRBs and BeXRBs, following the catalogue made by Fortin et al. (2023). Given the assumed $P_{\rm orb,\,SN}$ and ΔM, most binaries are consistent with the K96 limits.

Several caveats should be considered in interpreting the results. Even though K96 is agnostic to detailed kick mechanism, it does rely on the assumption of a Gaussian distribution for the kick velocity components; however, it is possible that the distribution might differ for different kick mechanisms. Moreover, it should also be noted that we use the universal log-linear fit across different binary types as a complementary method to test for negative correlation, so caution should be exercised in drawing very detailed conclusions about the underlying physical processes; with discoveries of more binaries in each type, type-specific analyses (e.g. with Bayesian hierarchical modelling) would certainly be helpful to explore different kick mechanisms.

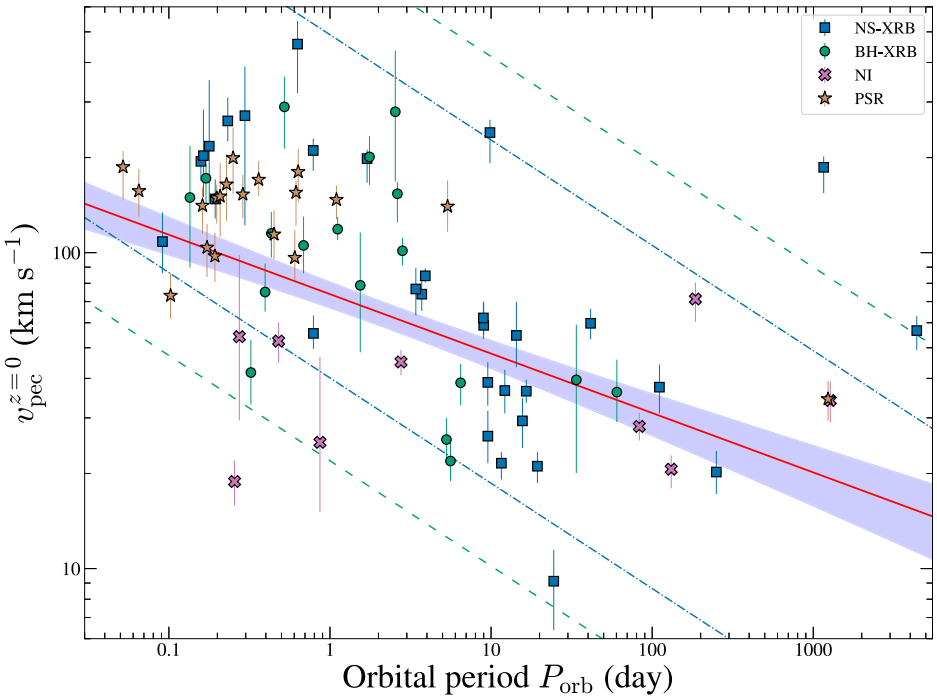

Figure 7. Scatter plot of $v_{\rm pec}^{z=0}$ and $P_{\rm orb}$ for binaries with measured $P_{\rm orb}$. The error bars on $v_{\rm pec}^{z=0}$ correspond to 16th and 84th percentiles from Table 3. The model with the median bootstrapped fit parameters is shown with the solid red line; the blue shading indicates the 68 per cent confidence region. The blue dashed-dotted line and green dashed line represent the K96 limits (as example trend lines) for a typical NS and BH-LMXB, respectively, assuming M_1 and ΔM in Table 8 and $M_2 = 0.5\,{\rm M}_\odot$.

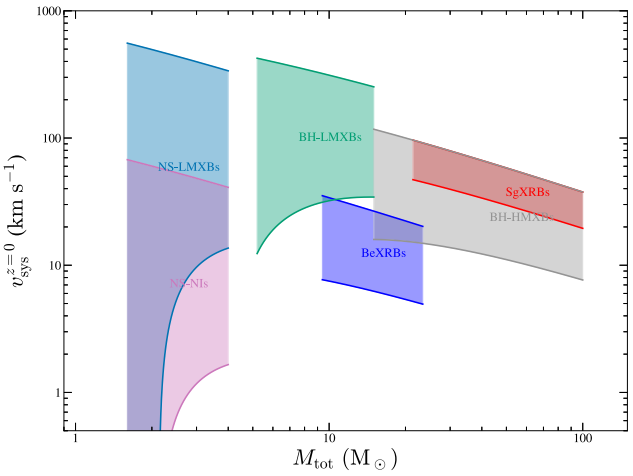

Figure 8. K96 limits [equation (9)] plotted for different binary types hosting NSs or BHs, using orbital parameters from Table 8. A general decreasing trend with $M_{\rm tot}$ is present despite each group having a range of possible $v_{\rm pec}^{z=0}$ values.

4.2 GX 1+4: a wide symbiotic X-ray binary with a high peculiar velocity

GX 1+4 is a rare case of symbiotic XRB where an NS is in a wide orbit ($P_{\rm orb} = 1160$ day) with a late-type giant (SyXRBs; Hinkle et al. 2006). In our compilation, it has a large $v_{\rm pec}^{z=0}$ ($\gtrsim 100\,{\rm km s^{-1}}$) that stands out in the upper right region of Fig. 7. A high $v_{\rm pec}^{z=0}$ could be a result of a strong NK, but this then contradicts its wide orbit that is prone to disruption by strong kicks. GX 1+4 does not have a well-measured *Gaia* parallax, so we adopt the distance estimate of 4.5 kpc in Hinkle et al. (2006). Indeed, its negative parallax indicates that the true parallax is very small, so the distance should be greater than 4.5 kpc (Bailer-Jones et al. 2021), which will further increase its $v_{\rm pec}^{z=0}$ value. As a comparison, another SyXRB, 4U 1700+24, has a wider orbit ($P_{\rm orb} = 4391$ day; Hinkle et al. 2019) but is less of an outlier considering that its $v_{\rm pec}^{z=0}$ is close to the velocity dispersion of the disc population ($\approx 40\,{\rm km s^{-1}}$; Carlberg et al. 1985).

There are multiple scenarios where wide SyXRBs can survive SNe. One possibility is that NSs in some SyXRB progenitors were formed through electron capture SNe (Miyaji et al. 1980; Nomoto 1984) or accretion-induced collapse (Freire & Tauris 2014). Theoetrical work suggests that these events generally impart low NKs on the NSs (Dessart et al. 2006; Kitaura, Janka & Hillebrandt 2006; Gessner & Janka 2018), despite the fact that population synthesis suggested that only a small fraction formed in this way (Lü et al. 2012).

Table 8. Typical parameters for different binary types used to plot K96 limits in Fig. 8.

Type	M_1 (M$_\odot$)	ΔM (M$_\odot$)	$P_{\rm orb,\,SN}$ (d)
NS-LMXB	1.4	1.0	1
BH-LMXB	5.0	6.0	10
BH-HMXB	5.0	6.0	100
SgXRB	1.4	5.0	10
BeXRB	1.4	2.0	300
NS-NI	1.4	1.0	560

Alternatively, the massive component (i.e. the NS progenitor) might have lost a considerable fraction of its envelope through a CE stage (Taam & Sandquist 2000), which in turn limits the amount of mass ejected in the following SNe and thus the Blauww kick. However, this is hard to reconcile with the observed high $v_{\rm pec}^{z=0}$ values based on either a weak kick or a small mass loss. Following the formulation of Nelemans et al. (1999), after a core-collapse SN, the ejecta mass has to be less than half of the total of helium core and companion mass to not disrupt the progenitor binary; if GX 1+4 starts in a compact binary at the SN with $P_{\rm orb,SN} = 10$ day, and if one assumes a helium core mass of $3\,{\rm M}_\odot$ and a companion mass of $1\,{\rm M}_\odot$ at SN, mass loss can only contribute a maximum of only $\approx 63\,{\rm km\,s^{-1}}$ to the $v_{\rm pec}^{z=0}$; then post-SN evolution will have to involve mechanisms that expand the orbit to match its present-day $P_{\rm orb}$. Fortuitous cases where the NS is accelerated by appropriately directed weak kicks might reconcile with the large $v_{\rm pec}^{z=0}$ but should be very rare.

Alternatively, GX 1+4's proximity to the Galactic centre might suggest that it is a binary born in the bulge. In this case, it would have been dynamically perturbed by the dense stellar population there, so its $v_{\rm pec}^{z=0}$ is not reflective of a NK. However, it is worth noting that SyXRBs with wide orbits are particularly susceptible to disruption due to dynamical encounters in dense environments (see e.g. Belloni et al. 2020). There have been no confirmed symbiotic stars in comparably dense globular clusters, although there is one controversial candidate (Henleywillis et al. 2018; Belloni et al. 2020).

4.3 Present-day orbital period versus peculiar velocity

Interpreting the anticorrelation with $P_{\rm orb}$ following K96 can be more complex. One could naively ascribe the decreasing trend in $v_{\rm pec}^{z=0}$ to the upper K96 limits that scale negatively with $P_{\rm orb,\,SN}$ (see Fig. 7); however, transposing from $P_{\rm orb,\,SN}$ to the present-day $P_{\rm orb}$ requires knowledge of (1) the kick magnitude and direction on the compact object, and (2) post-SN orbital evolution. Brandt & Podsiadlowski (1995, B95, hereafter) have conducted a systematic investigation of pre- and post-SN orbital parameters and found that most binaries have a post-SN orbital period ($P_{\rm orb,\,post\text{-}SN}$) close to $P_{\rm orb,\,SN}$ within a factor of a few (fig. 4a in B95). Additionally, B95 points out that among binaries that survived SNe, the ones with high $v_{\rm pec}$ values are preferentially those perturbed by NKs in approximately the *opposite* direction to the instantaneous orbital velocity of the compact objects; this can essentially decelerate the compact object and shrink the orbits, resulting in a decreasing trend with $P_{\rm orb,\,post\text{-}SN}$ (e.g. fig. 5b in B95).

After SNe, there are various mechanisms that can further change the orbital period. While $P_{\rm orb,\,post\text{-}SN}$ should be reasonably close to their present-day values for the HM binaries considering their young ages, the orbit of LM binaries (especially LMXBs) is dependent on the synergy of mass transfer and/or processes that dissipate angular momentum. The former sets in when the mass donor fills its Roche lobe due to nuclear evolution (sub-giant donors, e.g. Cyg X-2) or orbit shrinkage induced by angular momentum loss (main-sequence donors); the orbit tends to expand on thermal timescale under stable and conservative mass transfer. However, to maintain the donor's contact with its Roche lobe, mechanisms are needed to extract angular momentum from the system to counteract orbit expansion. The current consensus is that angular momentum can be dissipated via gravitational wave radiation (Faulkner 1971; Verbunt 1993) and/or magnetic braking (Rappaport, Verbunt & Joss 1983); the former only dominates in ultra-compact XRBs, while magnetic braking is considered effective in the majority of LMXBs. Over these processes, orbits can expand or shrink at the bifurcation period (≈ 1 d; Tutukov et al. 1985; Pylyser & Savonije 1988). Depending on the initial (at the onset of mass transfer) state of the donor and magnetic braking prescription, the overall mass transfer phase can modify the orbital period by up to $\approx$2 orders of magnitude (see e.g. Ergma & Sarna 1996; Podsiadlowski, Rappaport & Pfahl 2002; Van, Ivanova & Heinke 2019).

Despite this multitude of uncertainty, Fig. 7 still shows a significant anticorrelation. So while different evolutionary trajectories probably account for much of the scatter visible in the figure, these do not erase underlying properties linking binaries across the dynamic range of our sample. Fig. 7 thus provides a useful constraint for population synthesis models to satisfy. The strongest governing link is likely the system binding energy, with wider binaries being loosely bound and thus being more likely to be disrupted when $v_{\rm pec}^{z=0}$ is higher. Testing this hypothesis, however, will require proper characterization of XRB selection, combined with *Gaia*'s selection function (cf. Cantat-Gaudin et al. 2023), which is beyond the scope of the present work.

4.4 Possible biases

The $v_{\rm pec}^{z=0}$-$M_{\rm tot}$ and $v_{\rm pec}^{z=0}$-$P_{\rm orb}$ correlations could have been contributed by selection biases on our sample. It should be firstly noted that our compilation contains only NSs and BHs in *present-day* bound systems, which is not necessarily a representation of the binary demography at the instant of SNe. In part, either mass ejection or additional kicks would typically bias against wide binaries, which were more prone to being disrupted; NSs in very close pre-SN orbits, on the other hand, could be re-directed to collide with the companion and form Thorne–Żytkow objects (Thorne & Zytkow 1975, 1977).

Wide binaries are also prone to observational biases considering the difficulty of measuring long $P_{\rm orb}$. There is an obvious paucity of binaries above $P_{\rm orb} \approx 100$ day in Fig. 7: six binaries are present including two wide SyXRBs (Section 4.2), the NI binary Gaia BH2 (El-Badry et al. 2023a), the massive binary pulsar PSR B1259−63, and two HMXBs (1A 0535+262 and X Persi). Compact objects in NIs can only be confirmed by robust constraints on mass function, which in turn asks for multi-epoch observations spanning at least one full orbital period; for very long $P_{\rm orb}$'s, this could be time-expensive. Dedicated radial velocity campaign can therefore only be performed for a handful of well-justified cases, despite the fact that there might be a uncharted population of wide NIs (e.g. El-Badry et al. 2023a, b). Wide binaries can also be sought by searches for astrometric wobble with, e.g. Gaia (Gould & Salim 2002; Barstow et al. 2014).

There might also be more wide BeXRBs to be discovered (Vinciguerra et al. 2020). BeXRBs are mostly transient systems that exhibit periodic X-ray outbursts (Type I outbursts) that can be orders of magnitude brighter than their quiescence. Because these outbursts happen at roughly $P_{\rm orb}$, they can be used to measure their $P_{\rm orb}$. However, this relies on the consecutiveness of outburst detection, which is less feasible if $P_{\rm orb}$ is very long. Moreover, long $P_{\rm orb}$ might also restrict X-ray detectability, typically for wind-fed HMXBs. Identification of a NS in HMXBs can be assisted by detections of (accretion-induced) X-ray pulsations. However, at a given wind mass loss rate of the mass donor, X-ray luminosities of such binaries scale inversely with orbital separation (Bondi & Hoyle 1944), so wide systems would be more difficult to detect. Contrary

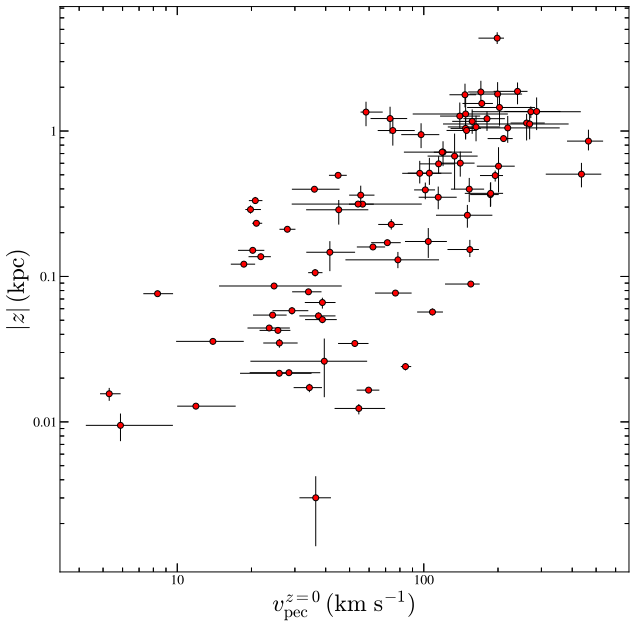

Figure 9. Galactic height $|z|$ vs. $v_{\rm pec}^{z=0}$ showing a clear positive correlation for binaries in Table 3. Error bars correspond to 16th and 84th percentiles.

to wind-fed HMXBs, thinner stellar wind in wide binaries could in favour discovery of more OB-pulsar binaries like PSR B1259−63. The NS nature in such binaries can be confirmed by detection of radio pulsations (Johnston et al. 1992; Lyne et al. 2015), which can otherwise be greatly smeared out by stronger stellar wind in more compact systems.

We have excluded binaries in globular clusters from our sample; however, it is possible that some of the LMXBs in our sample were formed in globular clusters but were later dynamically ejected. This can account for typically (ultra-)compact XRBs that are more likely to survive dynamical interactions in dense environment. Combining an escape velocity of 50 kms^{-1} (velocity relative to the cluster) and cluster velocity dispersion of 100–120 kms^{-1} (Vasiliev 2019) results in $v_{\rm pec,\,p}$ over 100 kms^{-1}; therefore, the high-velocity part of our sample might have been contaminated, although simulations only suggest a small number of such binaries (Kremer et al. 2018). Future metalicity measurements will provide information to further identify/discover these ejected systems.

Another observational bias involves the Galactic height ($|z|$) of binaries off the plane. We select the binaries based on robust identification of compact objects. This would require optical/near-IR visibility of the luminous component and would therefore bias against potential low-$v_{\rm pec}^{z=0}$ systems as they are less likely to reach large $|z|$ as the high-$v_{\rm pec}^{z=0}$ ones (Fig. 9) and therefore are more obscured by Galactic extinction (Gandhi et al. 2020; Jonker et al. 2021; Shikauchi et al. 2023). This bias could be typically strong against LM binaries that have faint components, e.g. LM-NIs, and is even worse for the low-$v_{\rm pec}^{z=0}$ LMXBs that formed through direct-SN (Kalogera 1998; Section 4.1), which could have populated the lower-left region of the $v_{\rm pec}^{z=0}$-$P_{\rm orb}$ plot. It will be interesting to constrain the extent to which these low-velocity binaries are affected by observational biases while exploring possible physical mechanisms that contribute to the lack of such binaries.

5 CONCLUSION

We compile a sample of 89 binaries that (1) host a NS or BH and (2) have measured astrometry and systemic radial velocities. We calculate their present-day peculiar velocities ($v_{\rm pec,\,p}$) and their extrapolated peculiar velocity at the Galactic disc ($v_{\rm pec}^{z=0}$), incorporating uncertainties in astrometric parameters and Galactic constants; these velocities are treated as their potential peculiar velocity at birth. The calculated velocity samples can be compared to simulated distributions in future population synthesis studies.

We perform statistical modelling of the overall distribution of $v_{\rm pec}^{z=0}$ and use K-S test to compare $v_{\rm pec}^{z=0}$ distributions between different subgroups. Our findings suggest no statistically significant difference between BH and NS binaries; however, we find that HM binaries are restricted to $v_{\rm pec}^{z=0}$ below ≈ 100 kms^{-1} while LM binaries exhibit a much wider distribution that goes up to ≈ 400 kms^{-1}. The difference is primarily contributed by NS binaries, while comparing BH-LM and HM binaries only suggest a moderate significance.

Fitting a log-linear model of $v_{\rm pec}^{z=0}$ versus $M_{\rm tot}$ results in a negative slopes at over 99.7 per cent confidence, while a similar log-linear fit to $v_{\rm pec}^{z=0}$ versus $P_{\rm orb}$ also shows a significant negative slope (at 99.7 per cent confidence). Both fits suggest a non-negligible fraction of additional uncertainty in $v_{\rm pec}^{z=0}$, with which both anticorrelations are slightly weakened but are still at robust levels. The anticorrelation between $v_{\rm pec}^{z=0}$ with $M_{\rm tot}$ follows the kinematic formulation derived by Kalogera (1996). Interpretation of the correlation with $P_{\rm orb}$ is complicated by uncertainty in underlying kick velocity distribution and binary evolution models, which would require more detailed population synthesis studies.

ACKNOWLEDGEMENTS

We thank the anonymous reviewer for their helpful feedback. This work has made use of data from the European Space Agency (ESA) mission *Gaia* (https://www.cosmos.esa.int/gaia), processed by the *Gaia* Data Processing and Analysis Consortium (DPAC, https://www.cosmos.esa.int/web/gaia/dpac/consortium). Funding for the DPAC has been provided by national institutions, in particular the institutions participating in the *Gaia* Multilateral Agreement. This research has also made use of the SIMBAD data base, operated at CDS, Strasbourg, France. PG, YZ, and CDB acknowledge the Science and Technology Facilities Council grant ST/V001000/1 for support.

Analysis and visualisation in this work have also made use of the following software packages: ASTROPY[8]: a community-developed core Python package and an ecosystem of tools and resources for astronomy (Astropy Collaboration 2022), MATPLOTLIB (Hunter 2007), NUMPY (Harris et al. 2020), and PANDAS (The pandas development team 2023).

DATA AVAILABILITY

The *Gaia* astrometry data are available by querying the *Gaia* archive. The calculated $v_{\rm pec,\,p}$ and $v_{\rm pec}^{z=0}$ samples are available upon request.

REFERENCES

Abubekerov M. K., Antokhina É. A., Cherepashchuk A. M., 2004, Astron. Rep., 48, 89

[8]http://www.astropy.org

Allen B. et al., 2013, ApJ, 773, 91
An H. et al., 2015, ApJ, 806, 166
Andrews J. J., Kalogera V., 2022, ApJ, 930, 159
Antoniadis J. et al., 2013, Science, 340, 448
Aragona C., McSwain M. V., De Becker M., 2010, ApJ, 724, 306
Aragona C., McSwain M. V., Grundstrom E. D., Marsh A. N., Roettenbacher R. M., Hessler K. M., Boyajian T. S., Ray P. S., 2009, ApJ, 698, 514
Archibald A. M., Kaspi V. M., Hessels J. W. T., Stappers B., Janssen G., Lyne A., 2013, preprint (arXiv:1311.5161)
Arnason R. M., Papei H., Barmby P., Bahramian A., Gorski M. D., 2021, MNRAS, 502, 5455
Arras P., Lai D., 1999, ApJ, 519, 745
Ashcraft T. A., Hynes R. I., Robinson E. L., 2012, MNRAS, 424, 620
Astropy Collaboration, 2022, ApJ, 935, 167
Atri P. et al., 2019, MNRAS, 489, 3116
Bailer-Jones C. A. L., Rybizki J., Fouesneau M., Demleitner M., Andrae R., 2021, AJ, 161, 147
Barstow M. A. et al., 2014, preprint (arXiv:1407.6163)
Barsukova E. A., Borisov N. V., Burenkov A. N., Klochkova V. G., Goranskij V. P., Metlova N. V., 2005, Astron. Telegram, 416, 1
Bassa C. G. et al., 2016, MNRAS, 460, 2207
Bates S. D. et al., 2015, MNRAS, 446, 4019
Bellm E. C. et al., 2016, ApJ, 816, 74
Belloni D., Mikołajewska J., Iłkiewicz K., Schreiber M. R., Giersz M., Rivera Sandoval L. E., Rodrigues C. V., 2020, MNRAS, 496, 3436
Belokurov V. et al., 2020, MNRAS, 496, 1922
Bikmaev I. F. et al., 2017, Astron. Lett., 43, 664
Bird A. J. et al., 2016, ApJS, 223, 15
Blaauw A., 1961, Bull. Astron. Inst. Netherlands, 15, 265
Bondi H., Hoyle F., 1944, MNRAS, 104, 273
Bovy J., 2015, ApJS, 216, 29
Brandt N., Podsiadlowski P., 1995, MNRAS, 274, 461
Brandt W. N., Podsiadlowski P., Sigurdsson S., 1995, MNRAS, 277, L35
Brisken W. F., Fruchter A. S., Goss W. M., Herrnstein R. M., Thorsett S. E., 2003, AJ, 126, 3090
Callanan P. J., Garnavich P. M., Koester D., 1998, MNRAS, 298, 207
Camilo F., Rasio F. A., 2005, in Rasio F. A., Stairs I. H.eds, Astronomical Society of the Pacific Conference Series, Vol. 328, Binary Radio Pulsars, Astron. Soc. Pac, San Francisco, p.147
Cantat-Gaudin T. et al., 2023, A&A, 669, A55
Cantrell A. G. et al., 2010, ApJ, 710, 1127
Carlberg R. G., Dawson P. C., Hsu T., Vandenberg D. A., 1985, ApJ, 294, 674
Casares J. et al., 2009, ApJS, 181, 238
Casares J., Charles P. A., 1994, MNRAS, 271, L5
Casares J., Cornelisse R., Steeghs D., Charles P. A., Hynes R. I., O'Brien K., Strohmayer T. E., 2006, MNRAS, 373, 1235
Casares J., Muñoz-Darias T., Mata Sánchez D., Charles P. A., Torres M. A. P., Armas Padilla M., Fender R. P., García-Rojas J., 2019, MNRAS, 488, 1356
Casares J., Ribó M., Ribas I., Paredes J. M., Martí J., Herrero A., 2005, MNRAS, 364, 899
Casares J., Ribó M., Ribas I., Paredes J. M., Vilardell F., Negueruela I., 2012, MNRAS, 421, 1103
Casares J., Steeghs D., Hynes R. I., Charles P. A., O'Brien K., 2003, ApJ, 590, 1041
Casares J., Zurita C., Shahbaz T., Charles P. A., Fender R. P., 2004, ApJ, 613, L133
Chakrabarti S. et al., , 2023, AJ, 166, 6
Cherepashchuk A. M., Khruzina T. S., Bogomazov A. I., 2021, MNRAS, 508, 1389
Chojnowski S. D. et al., 2017, AJ, 153, 174
Chugai N. N., 1984, Sov. Astron. Lett., 10, 87
Clark C. J. et al., 2021, MNRAS, 502, 915
Cornelisse R., Kotze M. M., Casares J., Charles P. A., Hakala P. J., 2013, MNRAS, 436, 910
Corral-Santana J. M., Casares J., Muñoz-Darias T., Bauer F. E., Martínez-Pais I. G., Russell D. M., 2016, A&A, 587, A61
Crampton D., Hutchings J. B., 1981, ApJ, 251, 604
Crampton D., Hutchings J. B., Cowley A. P., 1985, ApJ, 299, 839
Crawford F. et al., 2013, ApJ, 776, 20
Davison P. J. N., Watson M. G., Pye J. P., 1977, MNRAS, 181, 73
De Loore C., de Grève J. P., van den Heuvel E. P. J., de Cuyper J. P., 1974, Mem. Soc. Astron. Ital., 45, 893
de Martino D. et al., 2014, MNRAS, 444, 3004
Delgado-Martí H., Levine A. M., Pfahl E., Rappaport S. A., 2001, ApJ, 546, 455
Deller A. T. et al., 2012, ApJ, 756, L25
den Hartog P. R., Kuiper L. M., Corbet R. H. D., in't Zand J. J. M., Hermsen W., Vink J., Remillard R., van der Klis M., 2004, Astron. Telegram, 281, 1
Deneva J. S. et al., 2016, ApJ, 823, 105
Dessart L., Burrows A., Livne E., Ott C. D., 2006, ApJ, 645, 534
Dhawan V., Mirabel I. F., Rodríguez L. F., 2000, ApJ, 543, 373
Díaz Trigo M., Parmar A. N., Boirin L., Motch C., Talavera A., Balman S., 2009, A&A, 493, 145
Dorofeev O. F., Rodionov V. N., Ternov I. M., 1985, Sov. Astron. Lett., 11, 123
El-Badry K. et al., 2023a, MNRAS, 521, 4323
El-Badry K. et al., 2023b, MNRAS, 518, 1057
Ergma E., Sarna M. J., 1996, MNRAS, 280, 1000
Fabian A. C., Pringle J. E., Rees M. J., 1975, MNRAS, 172, 15
Falanga M., Bozzo E., Lutovinov A., Bonnet-Bidaud J. M., Fetisova Y., Puls J., 2015, A&A, 577, A130
Faulkner J., 1971, ApJ, 170, L99
Foreman-Mackey D. et al., 2016, The Journal of Open Source Software, 1, 24
Fortin F., García F., Chaty S., Chassande-Mottin E., Simaz Bunzel A., 2022, A&A, 665, A31
Fortin F., Garcia F., Simaz-Bunzel A., Chaty S., 2023, *A&A*, 671, A149
Fragos T., Willems B., Kalogera V., Ivanova N., Rockefeller G., Fryer C. L., Young P. A., 2009, ApJ, 697, 1057
Freire P. C. C., Tauris T. M., 2014, MNRAS, 438, L86
Fryer C. L., Belczynski K., Wiktorowicz G., Dominik M., Kalogera V., Holz D. E., 2012, ApJ, 749, 91
Fryer C. L., Kalogera V., 2001, ApJ, 554, 548
Fujita Y., Inoue S., Nakamura T., Manmoto T., Nakamura K. E., 1998, ApJ, 495, L85
Gaia Collaboration, 2016, A&A, 595, A1
Gaia Collaboration, 2023, *A&A*, 674, A1
Gamen R., Barbà R. H., Walborn N. R., Morrell N. I., Arias J. I., Maíz Apellániz J., Sota A., Alfaro E. J., 2015, A&A, 583, L4
Gandhi P. et al., 2022, MNRAS, 510, 3885
Gandhi P., Rao A., Charles P. A., Belczynski K., Maccarone T. J., Arur K., Corral-Santana J. M., 2020, MNRAS, 496, L22
Gandhi P., Rao A., Johnson M. A. C., Paice J. A., Maccarone T. J., 2019, MNRAS, 485, 2642
Gelman A., Rubin D. B., 1992, Stat. Sci., 7, 457
Gessner A., Janka H.-T., 2018, ApJ, 865, 61
Gies D. R. et al., 2008, ApJ, 678, 1237
Gies D. R., Bolton C. T., 1986, ApJS, 61, 419
Gomez S., Grindlay J. E., 2021, ApJ, 913, 48
Gontcharov G. A., 2006, Astron. Lett., 32, 759
González Hernández J. I., Casares J., 2010, A&A, 516, A58
González Hernández J. I., Rebolo R., Casares J., 2014, MNRAS, 438, L21
González Hernández J. I., Rebolo R., Israelian G., 2008a, A&A, 478, 203
González Hernández J. I., Rebolo R., Israelian G., Filippenko A. V., Chornock R., Tominaga N., Umeda H., Nomoto K., 2008b, ApJ, 679, 732
González Hernández J. I., Suárez-Andrés L., Rebolo R., Casares J., 2017, MNRAS, 465, L15
González-Galán A., Negueruela I., Castro N., Simón-Díaz S., Lorenzo J., Vilardell F., 2014, A&A, 566, A131

Gould A., Salim S., 2002, ApJ, 572, 944
Green G. M., 2018, J. Open Source Softw., 3, 695
Green G. M., Schlafly E., Zucker C., Speagle J. S., Finkbeiner D., 2019, ApJ, 887, 93
Gregory P. C., 2002, ApJ, 575, 427
Grundstrom E. D. et al., 2007a, ApJ, 656, 431
Grundstrom E. D. et al., 2007b, ApJ, 660, 1398
Gunn J. E., Ostriker J. P., 1970, ApJ, 160, 979
Habets G. M. H. J., 1985, PhD thesis, University of Amsterdam, Netherlands
Hambaryan V. et al., 2022, MNRAS, 511, 4123
Harlaftis E. T., Steeghs D., Horne K., Filippenko A. V., 1997, AJ, 114, 1170
Harris C. R. et al., 2020, Nature, 585, 357
Heida M., Jonker P. G., Torres M. A. P., Chiavassa A., 2017, ApJ, 846, 132
Henleywillis S., Cool A. M., Haggard D., Heinke C., Callanan P., Zhao Y., 2018, MNRAS, 479, 2834
Hills J. G., 1976, MNRAS, 175, 1P
Hinkle K. H., Fekel F. C., Joyce R. R., Mikołajewska J., Gałan C., Lebzelter T., 2019, ApJ, 872, 43
Hinkle K. H., Fekel F. C., Joyce R. R., Wood P. R., Smith V. V., Lebzelter T., 2006, ApJ, 641, 479
Hobbs G., Lorimer D. R., Lyne A. G., Kramer M., 2005, MNRAS, 360, 974
Hoffman M. D., Gelman A., 2011, preprint (arXiv:1111.4246)
Holland-Ashford T., Lopez L. A., Auchettl K., Temim T., Ramirez-Ruiz E., 2017, ApJ, 844, 84
Hunter J. D., 2007, Comput. Sci. Eng., 9, 90
Hutchings J. B., 1984, PASP, 96, 312
Hutchings J. B., Crampton D., Cowley A. P., Thompson I. B., 1987, PASP, 99, 420
Iaria R. et al., 2018, MNRAS, 473, 3490
Igoshev A. P., 2020, MNRAS, 494, 3663
Islam N., Paul B., 2016, MNRAS, 461, 816
Ivanova N., Heinke C. O., Rasio F. A., Belczynski K., Fregeau J. M., 2008, MNRAS, 386, 553
Janka H.-T., 2013, MNRAS, 434, 1355
Janka H.-T., 2017, ApJ, 837, 84
Jayasinghe T. et al., 2019, MNRAS, 486, 1907
Jennings R. J., Kaplan D. L., Chatterjee S., Cordes J. M., Deller A. T., 2018, ApJ, 864, 26
Johnston S., Manchester R. N., Lyne A. G., Bailes M., Kaspi V. M., Qiao G., D'Amico N., 1992, ApJ, 387, L37
Jonker P. G., Kaur K., Stone N., Torres M. A. P., 2021, ApJ, 921, 131
Jonker P. G., Nelemans G., 2004, MNRAS, 354, 355
Jonker P. G., Steeghs D., Nelemans G., van der Klis M., 2005, MNRAS, 356, 621
Jonker P. G., van der Klis M., 2001, ApJ, 553, L43
Kalogera V., 1996, ApJ, 471, 352, K96
Kalogera V., 1998, ApJ, 493, 368
Kaper L., van der Meer A., Najarro F., 2006, A&A, 457, 595
Kapil V., Mandel I., Berti E., Müller B., 2023, MNRAS, 519, 5893
Kaplan D. L. et al., 2016, ApJ, 826, 86
Kaplan D. L., Bhalerao V. B., van Kerkwijk M. H., Koester D., Kulkarni S. R., Stovall K., 2013, ApJ, 765, 158
Keane E. F. et al., 2018, MNRAS, 473, 116
Kharchenko N. V., Scholz R. D., Piskunov A. E., Röser S., Schilbach E., 2007, Astron. Nachr., 328, 889
Khargharia J., Froning C. S., Robinson E. L., 2010, ApJ, 716, 1105
Khargharia J., Froning C. S., Robinson E. L., Gelino D. M., 2013, AJ, 145, 21
Khokhlov S. A. et al., 2018, ApJ, 856, 158
Kimball C. et al., 2022, preprint (arXiv:2211.02158)
Kitaura F. S., Janka H. T., Hillebrandt W., 2006, A&A, 450, 345
Knigge C., Coe M. J., Podsiadlowski P., 2011, Nat., 479, 372
Kremer K., Chatterjee S., Rodriguez C. L., Rasio F. A., 2018, preprint (arXiv:1802.04895)
Kumar R., Carroll C., Hartikainen A., Martin O., 2019, J. Open Source Softw., 4, 1143
Lai D., 2004, in Höflich P., Kumar P., Wheeler J. C.eds, Cosmic Explosions in Three Dimensions: Asymmetries in Supernovae and Gamma-Ray Bursts, Cambridge University Press, Cambridge, p.276
Lam C. Y. et al., 2022, ApJ, 933, L23
LaSala J., Charles P. A., Smith R. A. D., Balucinska-Church M., Church M. J., 1998, MNRAS, 301, 285
LaSala J., Thorstensen J. R., 1985, AJ, 90, 2077
Lin J. et al., 2023, ApJ, 944, L4
Linares M., 2018, MNRAS, 473, L50
Linares M., Shahbaz T., Casares J., 2018, ApJ, 859, 54
Lindegren L. et al., 2021, A&A, 649, A4
Liu Q. Z., van Paradijs J., van den Heuvel E. P. J., 2006, A&A, 455, 1165, L06
Liu Q. Z., van Paradijs J., van den Heuvel E. P. J., 2007, A&A, 469, 807, L07
Lorimer D. R. et al., 2006, MNRAS, 372, 777
Lü G. L., Zhu C. H., Postnov K. A., Yungelson L. R., Kuranov A. G., Wang N., 2012, MNRAS, 424, 2265
Lyne A. G., Anderson B., Salter M. J., 1982, MNRAS, 201, 503
Lyne A. G., Lorimer D. R., 1994, Nat., 369, 127
Lyne A. G., Stappers B. W., Keith M. J., Ray P. S., Kerr M., Camilo F., Johnson T. J., 2015, MNRAS, 451, 581
Maccarone T. J., 2005, MNRAS, 360, L30
MacDonald R. K. D. et al., 2014, ApJ, 784, 2
Manchester R. N., Hobbs G. B., Teoh A., Hobbs M., 2005, AJ, 129, 1993
Mason K. O., Cordova F. A., 1982, ApJ, 262, 253
Mata Sánchez D., Muñoz-Darias T., Casares J., Jiménez-Ibarra F., 2017, MNRAS, 464, L41
Mata Sánchez D., Rau A., Álvarez Hernández A., van Grunsven T. F. J., Torres M. A. P., Jonker P. G., 2021, MNRAS, 506, 581
Mazeh T. et al., 2022, MNRAS, 517, 4005
Miller-Jones J. C. A. et al., 2018, MNRAS, 479, 4849
Miller-Jones J. C. A. et al., 2021, Sci., 371, 1046
Miller-Jones J. C. A., Jonker P. G., Dhawan V., Brisken W., Rupen M. P., Nelemans G., Gallo E., 2009, ApJ, 706, L230
Mirabel F., 2017, New Astron. Rev., 78, 1
Mirabel I. F., Dhawan V., Mignani R. P., Rodrigues I., Guglielmetti F., 2001, Nat., 413, 139
Miyaji S., Nomoto K., Yokoi K., Sugimoto D., 1980, PASJ, 32, 303
Moritani Y., Kawano T., Chimasu S., Kawachi A., Takahashi H., Takata J., Carciofi A. C., 2018, PASJ, 70, 61
Muñoz-Darias T., Casares J., Martínez-Pais I. G., 2005, ApJ, 635, 502
Nagase F., 1989, PASJ, 41, 1
Nelemans G., Tauris T. M., van den Heuvel E. P. J., 1999, A&A, 352, L87
Neustroev V. V., Veledina A., Poutanen J., Zharikov S. V., Tsygankov S. S., Sjoberg G., Kajava J. J. E., 2014, MNRAS, 445, 2424
Nicastro L., Lyne A. G., Lorimer D. R., Harrison P. A., Bailes M., Skidmore B. D., 1995, MNRAS, 273, L68
Nieder L. et al., 2020, ApJ, 902, L46
Nikolaeva E. A., Bikmaev I. F., Melnikov S. S., Galeev A. I., Zhuchkov R. Y., Irtuganov E. N., 2013, Bull. Crimean Astrophys. Obs., 109, 27
Nomoto K., 1984, ApJ, 277, 791
O'Doherty T. N., Bahramian A., Miller-Jones J. C. A., Goodwin A. J., Mandel I., Willcox R., Atri P., Strader J., 2023, MNRAS, 521, 2504
Orosz J. A. et al., 2001, ApJ, 555, 489
Orosz J. A. et al., 2002, ApJ, 568, 845
Orosz J. A., 2003, in van der Hucht K., Herrero A., Esteban C.eds, Vol. 212, A Massive Star Odyssey: From Main Sequence to Supernova, Astron. Soc. Pac., San Francisco, p. 365
Orosz J. A., Jain R. K., Bailyn C. D., McClintock J. E., Remillard R. A., 1998, ApJ, 499, 375
Orosz J. A., Steiner J. F., McClintock J. E., Torres M. A. P., Remillard R. A., Bailyn C. D., Miller J. M., 2011, ApJ, 730, 75

Paczynski B., 1976, in Eggleton P., Mitton S., Whelan J.eds, Proc. IAU Symp., 73, Structure and Evolution of Close Binary Systems, D. Reidel. p. 75
Pfahl E., Rappaport S., Podsiadlowski P., 2002a, ApJ, 573, 283
Pfahl E., Rappaport S., Podsiadlowski P., Spruit H., 2002b, ApJ, 574, 364
Picchi P., Shore S. N., Harvey E. J., Berdyugin A., 2020, A&A, 640, A96
Pletsch H. J., Clark C. J., 2015, ApJ, 807, 18
Plotkin R. M., Bahramian A., Miller-Jones J. C. A., Reynolds M. T., Atri P., Maccarone T. J., Shaw A. W., Gandhi P., 2021, MNRAS, 503, 3784
Podsiadlowski P., Langer N., Poelarends A. J. T., Rappaport S., Heger A., Pfahl E., 2004, ApJ, 612, 1044
Podsiadlowski P., Rappaport S., Pfahl E. D., 2002, ApJ, 565, 1107
Ponti G., Bianchi S., Muñoz-Darias T., Nandra K., 2018, MNRAS, 481, L94
Premachandra S. S., Galloway D. K., Casares J., Steeghs D. T., Marsh T. R., 2016, ApJ, 823, 106
Priedhorsky W. C., Terrell J., 1983, ApJ, 273, 709
Pylyser E., Savonije G. J., 1988, A&A, 191, 57
Ransom S. M. et al., 2014, Nat., 505, 520
Rappaport S., Verbunt F., Joss P. C., 1983, ApJ, 275, 713
Ray P. S. et al., 2012, preprint (arXiv:1205.3089)
Ray P. S., Chakrabarty D., 2002, ApJ, 581, 1293
Reardon D. J. et al., 2021, MNRAS, 507, 2137
Reid M. J. et al., 2009, ApJ, 700, 137
Reid M. J. et al., 2014a, ApJ, 783, 130
Reid M. J., McClintock J. E., Steiner J. F., Steeghs D., Remillard R. A., Dhawan V., Narayan R., 2014b, ApJ, 796, 2
Reig P., Chakrabarty D., Coe M. J., Fabregat J., Negueruela I., Prince T. A., Roche P., Steele I. A., 1996, A&A, 311, 879
Reig P., Fabregat J., Coe M. J., Roche P., Chakrabarty D., Negueruela I., Steele I., 1997, A&A, 322, 183
Remillard R. A., Orosz J. A., McClintock J. E., Bailyn C. D., 1996, ApJ, 459, 226
Reynolds A. P., Quaintrell H., Still M. D., Roche P., Chakrabarty D., Levine S. E., 1997, MNRAS, 288, 43
Romani R. W., 2012, ApJ, 754, L25
Romani R. W., Filippenko A. V., Cenko S. B., 2014, ApJ, 793, L20
Romani R. W., Filippenko A. V., Silverman J. M., Cenko S. B., Greiner J., Rau A., Elliott J., Pletsch H. J., 2012, ApJ, 760, L36
Romani R. W., Shaw M. S., 2011, ApJ, 743, L26
Russell T. D. et al., 2015, MNRAS, 450, 1745
Russell T. D., Soria R., Motch C., Pakull M. W., Torres M. A. P., Curran P. A., Jonker P. G., Miller-Jones J. C. A., 2014, MNRAS, 439, 1381
Sahu K. C. et al., 2022, ApJ, 933, 83
Salvatier J., Wieckiâ T. V., Fonnesbeck C., 2016, Astrophysics Source Code Library, record ascl:1610.016
Sanpa-Arsa S., 2016, PhD thesis, University of Virginia
Sarty G. E. et al., 2009, MNRAS, 392, 1242
Shahbaz T., 2003, MNRAS, 339, 1031
Shahbaz T., Watson C. A., Dhillon V. S., 2014, MNRAS, 440, 504
Shaw A. W., Charles P. A., Casares J., Hernández Santisteban J. V., 2016, MNRAS, 463, 1314
Shikauchi M., Tsuna D., Tanikawa, A., Kawanaka N., 2023, preprint (arXiv:2301.07207)
Smits M., Maccarone T. J., Kundu A., Zepf S. E., 2006, A&A, 458, 477
Steeghs D., Casares J., 2002, ApJ, 568, 273
Steeghs D., Jonker P. G., 2007, ApJ, 669, L85
Steeghs D., McClintock J. E., Parsons S. G., Reid M. J., Littlefair S., Dhillon V. S., 2013, ApJ, 768, 185
Stevens J. B., Reig P., Coe M. J., Buckley D. A. H., Fabregat J., Steele I. A., 1997, MNRAS, 288, 988
Stickland D., Lloyd C., Radziun-Woodham A., 1997, MNRAS, 286, L21
Storm J., Carney B. W., Gieren W. P., Fouqué P., Latham D. W., Fry A. M., 2004, A&A, 415, 531
Stovall K. et al., 2014, ApJ, 791, 67
Strader J. et al., 2019, ApJ, 872, 42
Strader J., Chomiuk L., Cheung C. C., Salinas R., Peacock M., 2015, ApJ, 813, L26
Swihart S. J., Strader J., Chomiuk L., Shishkovsky L., 2019, ApJ, 876, 8
Taam R. E., Sandquist E. L., 2000, ARA&A, 38, 113
Tanikawa A., Hattori K., Kawanaka N., Kinugawa T., Shikauchi M., Tsuna D., 2023, ApJ, 946, 79
The pandas development team, 2023, in pandas-dev/pandas: Pandas. Zenodo. Available at: https://doi.org/10.5281/zenodo.7979740
Thompson T. A. et al., 2019, Sci., 366, 637
Thorne K. S., Zytkow A. N., 1975, ApJ, 199, L19
Thorne K. S., Zytkow A. N., 1977, ApJ, 212, 832
Thorstensen J. R., Armstrong E., 2005, AJ, 130, 759
Torres M. A. P., Casares J., Jiménez-Ibarra F., Álvarez-Hernández A., Muñoz-Darias T., Armas Padilla M., Jonker P. G., Heida M., 2020, ApJ, 893, L37
Torres M. A. P., Casares J., Jiménez-Ibarra F., Muñoz-Darias T., Armas Padilla M., Jonker P. G., Heida M., 2019, ApJ, 882, L21
Trimble V., 1971, in Davies R. D., Graham-Smith F.eds, IAU Symp. 46, The Crab Nebula, D. Reidel. p. 12
Tutukov A. V., Fedorova A. V., Ergma E. V., Yungelson L. R., 1985, Sov. Astron. Lett., 11, 52
van den Heuvel E. P. J., Heise J., 1972, Nature Phys. Sci., 239, 67
van den Heuvel E. P. J., Portegies Zwart S. F., Bhattacharya D., Kaper L., 2000, A&A, 364, 563
van der Hooft F., Heemskerk M. H. M., Alberts F., van Paradijs J., 1998, A&A, 329, 538
van der Meer A., Kaper L., van Kerkwijk M. H., Heemskerk M. H. M., van den Heuvel E. P. J., 2007, A&A, 473, 523
Van K. X., Ivanova N., Heinke C. O., 2019, MNRAS, 483, 5595
van Staden A. D., Antoniadis J., 2016, ApJ, 833, L12
Vasiliev E., 2019, MNRAS, 484, 2832
Vehtari A., Gelman A., Gabry J., 2017, Stat. Comput., 27, 1413
Verbiest J. P. W., Weisberg J. M., Chael A. A., Lee K. J., Lorimer D. R., 2012, ApJ, 755, 39
Verbunt F., 1993, ARA&A, 31, 93
Verbunt F., Igoshev A., Cator E., 2017, A&A, 608, A57
Verbunt F., van den Heuvel E. P. J., 1995, in X-ray Binaries, Cambridge University Press, Cambridge, p. 457
Vinciguerra S. et al., 2020, MNRAS, 498, 4705
Virtanen P. et al., 2020, scipy/scipy: SciPy 1.5.3, Zenodo,
Waisberg I. R., Romani R. W., 2015, ApJ, 805, 18
Wang L., Steeghs D., Casares J., Charles P. A., Muñoz-Darias T., Marsh T. R., Hynes R. I., O'Brien K., 2017, MNRAS, 466, 2261
Waters L. B. F. M., Pols O. R., Hogeveen S. J., Cote J., van den Heuvel E. P. J., 1989, A&A, 220, L1
Williams S. J., Gies D. R., Matson R. A., Touhami Y., Grundstrom E. D., Huang W., McSwain M. V., 2010, ApJ, 723, L93
Wu J. et al., 2015, ApJ, 806, 92
Wu J., Orosz J. A., McClintock J. E., Hasan I., Bailyn C. D., Gou L., Chen Z., 2016, ApJ, 825, 46
Yao J. M., Manchester R. N., Wang N., 2017, ApJ, 835, 29
Yi T. et al., 2022, Nature Astron., 6, 1203
Yuan H. et al., 2022, ApJ, 940, 165
Zheng L.-L. et al., 2022, preprint (arXiv:2210.04685)
Zurita C., Durant M., Torres M. A. P., Shahbaz T., Casares J., Steeghs D., 2008, ApJ, 681, 1458

SUPPORTING INFORMATION

Supplementary data are available at *MNRAS* online.

Figure S1. Galactic map of binaries that host a BH.

Figure S2. The same as Fig. S1 but plotted for binaries hosting a NS.

Figure S3. Probability density distribution of $v_{\rm pec}^{z=0}$ of HMXBs, sorted by their medians.

Figure S4. The same as Fig. S3, but plotted for $v_{\rm pec}^{z=0}$ of LMXBs.

Figure S5. The same as Fig. S3, but plotted for $v_{\rm pec}^{z=0}$ of PSRs.

Figure S6. The same as Fig. S3, but plotted for $v_{\rm pec}^{z=0}$ of NI binaries.

Table S1. Literature distances ($d_{\rm lit}$)

Please note: Oxford University Press is not responsible for the content or functionality of any supporting materials supplied by the authors. Any queries (other than missing material) should be directed to the corresponding author for the article.

This paper has been typeset from a TEX/LATEX file prepared by the author.